CMT2A alleles with different effects on mitochondrial fusion share altered mitochondrial distribution and mitofusin turnover

Authors:

Olena O. Varuk [1], Amandine Ruiz [1], Célia Orengo[1], Amélie Cozzolino[1], Paul de Boissier [1], Aïcha Aouane[1], Thomas Rival [1§]

[1] Affiliation: Aix-Marseille Université, CNRS, IBDM, UMR 7288, F-13288 Marseille, France

[§] Correspondence: thomas.rival@univ-amu.fr

Abstract

Charcot-Marie-Tooth type 2A neuropathy (CMT2A) is caused by nearly one hundred missense mutations in the mitochondrial fusion factor mitofusin (Mfn). We showed that mutation hotspots target different structural motifs with functional significance for Mfn2. We then asked whether these mutations could differentially affect Mfn activity by comparing fourteen CMT2A alleles in drosophila. Based on specific changes in mitochondrial architecture, we grouped these alleles into four phenotypic classes. In particular, we identified dominant-negative alleles of variable strength, generally associated with catalytic motifs and hydrophobic cores, and active alleles favouring mitochondrial fusion, mostly located at the interface between domains. The cytoplasmic distribution of mitochondria was disturbed to varying degrees by the CMT2A alleles, associated with reduced endoplasmic reticulum-mitochondria overlap and fewer mitochondria at neuromuscular junctions. The heterogeneity of mitochondrial repartition was a major driver of neurotoxicity, correlating with the level of locomotor impairment measured in mutant flies and the disease severity in patients. At the molecular scale, most mutants showed reduced ubiquitination and increased basal levels of Mfn, likely contributing to their dominant properties. In conclusion, the CMT2A alleles induce an unexpected diversity of Mfn alterations in flies with general consequences on mitochondrion distribution and mutant protein level.

Introduction

Mitochondria are connected and disconnected by fusion-fission cycles. This process is mediated by conserved dynamin-related proteins (Tilokani et al., 2018) and supports mitochondrial homeostasis (Giacomello et al., 2020). The fusion of the outer and inner mitochondrial membranes (OMM, IMM) is driven respectively by mitofusin (Mfn) and OPA1. The resulting content mixing optimises and balances mitochondrial metabolism (Chen et al., 2005), buffers mitochondrial damage (Ono et al., 2001) and supports mitochondrial DNA replication (Silva Ramos et al., 2019). Mitochondrial fission is driven by DRP1 and facilitates mitophagy (Twig et al., 2008) and mitochondrial transport (Verstreken et al., 2005). Neurons, which are highly dependent on mitochondrial activity and transport, are susceptible to mitochondrial fusion-fission imbalances leading to neurological disorders (Bertholet et al., 2016, Tilokani et al., 2018). In particular, mutations affecting the ubiquitous protein Mfn2 cause type 2A Charcot-Marie-Tooth disease (CMT2A), a hereditary motor and sensory neuropathy (Stuppia et al., 2015). Most CMT2A cases are due to dominant alleles leading to amino acid (a.a.) substitutions (Stuppia et al., 2015, Pipis et al., 2020), although some recessive forms were described with deletions or a.a. substitutions present as heteroallelic combinations. Depending on the CMT2A alleles, early and late onset forms with severe or moderate symptoms have been described (Stuppia et al., 2015, Pipis et al., 2020).

Mfns are large multi-domain protein whose topology was predicted from that of the bacterial dynamin BDLP (Low and Lowe, 2006, Low et al., 2009). Mfns contain a GTP-binding domain (GTP-BD) and two helix bundles (HB1 and HB2) that are linked together by hinges. A short hydrophobic transmembrane segment (TM) anchors the protein to the OMM. HB1 and HB2 display two heptad repeats namely HR1 and HR2 forming a coiled coil. Resolved structures of truncated Mfn1 and Mfn2 (Koshiba et al., 2004, Cao et al., 2017, Yan et al., 2018, Li et al., 2019) and *in silico* modelling of Mfn2 (Beresewicz et al., 2018, Rocha et al., 2018) and yeast Mfn (Fzo1) (De Vecchis et al., 2019) have provided insights into the conformational changes that might mediate OMM fusion. Interactions through HR2 and/or GTP-BD might drive trans oligomerization and subsequent mitochondrial tethering (Cao et al., 2017, Li et al., 2019). At the hinges, GTP hydrolysis would then drive an upward GTP-BD tilt with respect to HB1 (Yan et al., 2018, Li et al., 2019) and a scissor-like movement bringing HB1 closer to HB2 (Beresewicz et al., 2018, Rocha et al., 2018, Brandner et al., 2019). This switch from an óopenô to a óclosedô conformation would provide the driving force for lipid bilayer fusion (Formosa and Ryan, 2016, De Vecchis et al., 2019). In this process, HR1 ï HR2 interaction might

negatively regulate fusion (Franco et al., 2016, Rocha et al., 2018) and contribute to lipid bilayers destabilisation (Daste et al., 2018). At the mitochondrial scale, studies in yeast showed that Mfns arrange into a docking ring mediating local membrane fusion through repeated cycles of GTP hydrolysis (Brandt et al., 2016). Mfns are regulated by phosphorylation, oxidation and ubiquitination (Giacomello et al., 2020). In yeast, Fzo1 turnover and oligomer disassembly are mediated by ubiquitination and subsequent proteasome-mediated degradation (Cohen et al., 2008, Alsayyah et al., 2020). In animals, several E3 ubiquitin ligases ubiquitinate Mfns, particularly in the context of stress-induced mitophagy (Escobar-Henriques and Joaquim, 2019). In addition, to their role in mediating mitochondrial fusion, Mfns are implicated in establishing contact sites between mitochondria and various organelles (Gordaliza-Alaguero et al., 2019, Alsayyah et al., 2024).

In Drosophila, mitochondria are dynamic and their fusion and fission machinery is supported by the same dynamin-like components than in mammals. Flies have two Mfns, sperm specific Fzo and ubiquitous MARF (Hwa et al., 2002) whose depletion in neurons triggers mitochondrial fragmentation (El Fissi et al., 2018). Like mammalian Mfns, MARF is regulated by ubiquitination (Ziviani et al., 2010, Yun et al., 2014) and oxidation (Smith et al., 2019). MARF restores mitochondrial fusion in *Mfn1-Mfn2* knockout mouse cells demonstrating the functional conservation between mammalian and insect Mfns (El Fissi et al., 2018). MARF appears closer to human Mfn2 than Mfn1 as the isoleucine 108 in G2 motif, responsible for Mfn1ôs tenfold higher GTPase activity, is replaced by a threonine in both Mfn2 (T129) and MARF (T170) (Li et al., 2019). In addition, MARF depletion somehow regulates ER-mitochondrion interactions (Debattisti et al., 2014, Sandoval et al., 2014), a Mfn2-specific function.

It is well known that the CMT2A mutations target residues distributed in the different Mfn2 domains (Cartoni and Martinou, 2009). To go further, we mapped all reported CMT2A mutations to models of Mfn2 protein structure. This revealed that CMT2A mutations are preferentially associated with structural motifs that were implicated in Mfn function. Given the complexity of Mfn structure and activity, we hypothesised that the CMT2A alleles might alter Mfn in different ways. To answer this *in vivo*, we used drosophila as a test tube. Fourteen alleles affecting different mutation hotspots were mimicked in MARF. Our work, involving the largest number of CMT2A alleles ever compared *in vivo*, revealed a broad spectrum of allele-specific mitochondrial alterations with a variety of phenotypes of varying severity.

Results

CMT2A mutations concentrate into structural hotspots

To highlight mutations hotspots in human Mfn2, we generated protein structure models based on BDLP closed and open conformations, onto which we mapped all CMT2A mutations (Fig. 1A,B). From the literature, we listed ninety-four Mfn2 residues mutated in CMT2A: 56% in GTP-BD, 22% in HB1, 11% in HB2, 7% in the hinges and 2% in the TM (Fig. 1A,B). Mutation frequency heat maps showed enrichment in specific structural motifs with functional significance (Fig. 1C,D,E and Supplementary Fig. 1A). The secondary structures at the front of GTP-BD were more affected than those at the back, particularly catalytic site G1, G2, G3 and G4 motifs, and Ŭ1G, Ŭ2G, Ŭ3G and Ŭ4G helices (Fig. 1C,D,E). The mutations affecting these regions may affect GTPase activity and oligomerisation, as homologous secondary structures in Mfn1 form the dimer interface (Supplementary Fig. 1B). In addition, the Ŭ3G Cter portion and the adjacent loop could form a GTP-BD ï HB1 interface in the Mfn2 open conformation as observed specifically in Mfn1 GTP-bound state (Fig. 1C and Supplementary Fig. 1B,C) whereas Ŭ2G and Ŭ3G could be involved in GTP-BD ï HB2 interactions in model of Mfn2 closed conformation (Fig. 1D). Mutations in these regions could affect transition between open and closed conformation. In HB1 and HB2, CMT2A mutations concentrated in Ŭ3H1 and Ŭ4H1 (Fig. 1C,D) that are part of HR1 and HR2 involved in oligomerisation and fusion activity. Finally, the hinges that support Mfn conformational changes are largely affected (Fig. 1C,D). Between GTP-BD and HB1, residues R94, R95, T356, K357 and S352 are mutated (Fig. 1A). The homologous Mfn1 residues are all involved in hinge 2 bending supporting GTP-BD movements upon GTP binding and hydrolysis (Supplementary Fig. 1B,C). The putative hinge bridging HB1 to HB2 is also targeted by CMT2A mutations, potentially affecting the transition between Mfn2 open and closed conformations (Fig. 1A,B,D,C). In conclusion, CMT2A mutation target regions of functional importance and may lead to different molecular outcomes.

Modelling CMT2A allele diversity in flies

To compare CMT2A alleles from different hotspots, we mimicked them in drosophila MARF. MARF and Mfn2 share 45.5% of identical a.a. and 15.2% with similar properties (Supplementary Fig. 2A,B). When only considering the residues mutated in CMT2A, identity and similarity were higher, 60.6% and 13.8% respectively (Supplementary Fig. 2A,B), reinforcing the idea that CMT2A residues are part of motifs critical for structure-function

relationships. For our study in flies, we selected fourteen a.a. substitutions affecting conserved residues in different hotspots: R104W, H128R and R259L for G1, G2 and G4 ; D214N for Ŭ2G ; L248V and R250Q for Ŭ3G-ƀ5G ; R94W and K357N for hinge 2 ; L92P for Ŭ2H ; H361Y, R364W and R400P for HR1 ; W740S and L745P for HR2 (Fig. 1F). This list included residues at Mfn2 surface, at the interface between two domains or buried within a domain. In selecting these residues, we checked that their localisation relative to protein domains and their lateral chain orientation were conserved in models of MARF (Supplementary Fig. 3A,B,F) and in available resolved structures of truncated Mfn2 and Mfn1 (Yan et al., 2018, Li et al., 2019). HB2 being unknown, we could not analyse R400. From there, a ódô prefix will refer to the MARF residues (MARF, Mfn2, Mfn1 correspondence: Supplementary Fig. 2C). As for human Mfn2, dR104, dH128 and dR259 localised in G2, G1 and G4 (Supplementary Fig. 3D and Fig. 4A) and are at the dimer interface, only dR259 being in a position to make hydrogen bonds as for Mfn1 (Supplementary Fig. 4B). The surface orientation of dW740, that is part of a coiled coil involved in oligomerisation (Koshiba et al., 2004) is also conserved (Supplementary Fig. 3E and Fig. 4C,E). In contrast to their orientation in the GDP-bound state (Supplementary Fig. 4C), the dR94, dR250, dK357 and dR364 lateral chains were at the GTP-BD ï HB1 interface in the GTP-bound state as for human Mfns (Fig. 3C, Fig. 4D). Of note, in MARF and Mfn2 close conformation models, D214/dD214 and R364/dR364 face HB2 (Fig. 1F, Supplementary Fig. 3B). Finally, GTP-BD residue dL248 (Supplementary Fig. 4F) and HB1 residues dL92, dH361 and dL745 (Supplementary Fig. 3E and Fig. 4E) associated with hydrophobic cores as for their Mfn2 counterparts. In building our allelic series, we also explored differences in pathogenicity. We included nine severe early onset alleles (L92P, R94W, R104W, H128R, K357N, H361Y, R364W, R400P), tree moderate late onset alleles (R259L, W740S, L745P) and two weak alleles proposed to be semi-dominant (D214N, R250Q) (Nicholson et al., 2008, Piscosquito et al., 2015, Tomaselli et al., 2016). We introduced these fourteen a.a. substitutions into the *marf* coding sequence, inserted all transgenes at the same genomic location and expressed them in neurons (Supplementary Fig. 5A). A wild-type control transgene, referred as *marfWT*, was similarly generated and provided an expression equivalent to 1.5 times that of endogenous MARF (Supplementary Fig. 5B). Wild type and mutant *marf* constructs were tagged with HA for specific immuno-detection.

The CMT2A mutants alter Mfn activity in different manners

We then imaged mitochondrial networks in living larval central nervous system (CNS) using high-resolution confocal microscopy and transmission electron microscopy (TEM). Consistent

with a balanced fusion-fission equilibrium, wild type motor neuron cell bodies contained both filamentous and fragmented mitochondria (Fig. 2A, Ø). Expression of the *marfWT* control transgene decreased mitochondrial fragmentation and triggered the over-fusion of mitochondrial filaments into net-like structures (Fig. 2A, *marfWT*). On the opposite, *marf* knockout caused a mitochondrial fragmentation rescued by *marf* re-expression (Fig. 2B, *marfKO*). To reveal CMT2A allele dominant properties, we analysed mitochondria in the presence of endogenous MARF. The resulting phenotypes were complex and composite (Fig. 2A, Supplementary Fig. 6). Therefore, we scored three categories of mitochondrial shape i.e. fragmented, filamentous and enlarged, and two modes of interaction i.e. net-like and clustered (Fig. 3A). In parallel, we evaluate the fusion capacity of each mutant in a *marfKO* background (Fig. 2B, Supplementary Fig. 7) by measuring the length of mitochondrial tubules (Fig. 3B). Then, the data in wild type and *marfKO* backgrounds were analysed using a hierarchical clustering (Fig. 3C). This allowed us to group our mutants into four allelic classes and to evaluate their phenotypic distance from wild type, *marfKO* and *marfWT* overexpressing flies. The mutant classes were named óGrapeô, óTangleô, óBulbô and óPeanutô according to the shape of their mitochondria (Fig. 2A). In the Grape group, which includes *dR94W*, *dR104W* and *dH128R*, motor neurons contained one or two large and spherical clusters of fragmented mitochondria that often showed IMM swirls or cristae loss (Fig. 2A, Fig. 3A and Supplementary Fig. 6B). Photoconversion experiments using mit::dendra2 showed that, despite being packed, mitochondria were not connected (Fig. 2D). Grape alleles did not restore tubules in *marfKO* animals, showing clusters of fragmented mitochondria (Fig. 2B, Fig. 3B and Supplementary Fig. 7B). Taken together, these data demonstrated that Grape mutations are strong dominant negatives (DN) that do not affect Mfn tethering but abolish the fusion capacity of wild-type Mfn. Consistently, Grape mutants were the closest to *marfKO* (Fig. 3C). In the Tangle alleles *dL92P*, *dL248V*, *dR259L* and *dH361Y*, we observed elongated clusters made of tightly packed mitochondrial tubules (Fig. 2A, Fig. 3A and Supplementary Fig. 6C). However, these mitochondria did not form an interconnected network as revealed by photoconversion experiments (Fig. 2D). In *marfKO* neurons, Tangle mitochondria remained largely fragmented although few very short tubules could be detected (Fig. 2B, Fig. 3B, Supplementary Fig. 7C). Hierarchical clustering placed Tangle close to Grape and *marfKO* (Fig. 2C). In conclusion, the Tangle mutants act as weak DN that essentially cluster mitochondria without abolishing endogenous MARF fusion capacity. In Peanut mutants *dR250Q* and *dL745P*, mitochondria essentially conserved their wild type shape (Fig. 2A, Fig. 3A, Supplementary Fig. 6D). Because some *dR250Q* neurons contained net-like mitochondria (Fig. 3A), we quantified mitochondrial

length and branching to detect subtle activity in the Peanut mutants. This revealed that *dR250Q*, and to a lesser extent *dL745P*, have a residual fusion capacity that was however much lower than the one of *marfWT* (and Fig. S8A-D). Consistently, analysis in *marfKO* neurons showed that *dR250Q* restored mitochondrial tubule formation, whereas *dL745P* only formed very scarce short elongated mitochondria (Fig. 2B, Fig. 3B and Supplementary Fig. 7D). Consistent with their phenotypes, Peanut alleles segregated with wild type control, *dR250Q* being the closest one (Fig. 2C). A fourth group, including *dD214N*, *dK357N*, *dR364W* and *dW740S*, formed bulb-like structures corresponding to enlarged mitochondria with normal cristae and no swelling (Fig. 2A, Fig. 3A and Supplementary Fig. 6E). These abnormal mitochondria were generally disconnected to the rest of the mitochondrial network, except for *dD214N* (Fig. 2C). The Bulb alleles restored mitochondrial tubules in *marfKO* cells and contained less fragmented mitochondria than the *marfWT* rescue (Fig. 2B, Fig. 3B and Supplementary Fig. 7E). In agreement with these observations, Bulb alleles segregated with flies overexpressing *marfWT* (Fig. 2C). In conclusion, Bulb alleles have dominant properties that switch the fusion/fission balance toward fusion. Regarding structure-function relationship, the mutant mitochondrial phenotypes did not correlate with specific protein domains (Fig. 2C). However, most fusion-incompetent alleles affected catalytic motifs and hydrophobic cores whereas most fusion-competent mutants affected interfaces between domains (Fig. 2C). Finally, we noticed that the alleles that clustered the closest to fusion-competent controls, i.e. *dD214N*, *dR250Q* and *dL745P*, consistently cause mild forms of CMT2A in human (Fig. 2C). In conclusion, our observations demonstrated that *marf* alleles mimicking CMT2A mutations can have different consequences on Mfn activity.

Variable extent of toxicity in CMT2A flies correlates with disease severity in patients

We then determined whether the mitochondrial abnormalities translate into neurotoxicity in flies. To that purpose, we analysed developmental lethality, photoreceptor neurodegeneration and locomotor performance upon neuron-specific expression of the CMT2A alleles. Of note, we measured startle-induced locomotion that is independent on vision (Supplementary Fig. 9). Consistent with their strong DN activity, Grape mutants were the most severely affected. Only few escapers reached adulthood exhibiting high photoreceptor loss and very poor locomotor ability (Fig. 4A,B,C). Tangle and Bulb phenotype expressivity varied between alleles with higher development lethality, stronger neurodegeneration and lower locomotion in *dL248V*, *dL92P* and *dH361Y* for Tangle and *dR364W* and *dK357N* for Bulb (Fig. 4A,B,C). Finally, Peanut mutants had no significant toxicity consistent with their mitochondrial phenotype (Fig.

4A,B,C). Importantly for disease relevance, *marf* alleles with weaker to no detectable neurotoxicity in flies corresponded to mutations known to cause moderate forms of CMT2A disease (*dR259L, dW740S* and *dL745P*) and to act as semi-dominant alleles in patients (*dD214N, dR250Q*). In conclusion, whereas the Grape and Peanut phenotypes correlated well with neurotoxicity level, Tangle and Bulb alterations had very variable degrees of toxicity.

Neurotoxicity correlates with altered mitochondrial distribution

Consistent with the above observations, only two mitochondrial traits correlated with decreased locomotor performance, the presence of clustered mitochondria and the loss of tubular ones (Supplementary Table 1).To understand the variable extent of neurotoxicity found within our allelic series, we searched for a common factor which strength could vary between alleles. An obvious parameter to look at was the distribution of mitochondria within motor neuron soma. Indeed, distribution could be altered both by the clustering observed in Grape and Tangle and by the hyperfusion of Bulb. Quantification revealed that mitochondria were homogeneously distributed in control as well as in Peanut mutants, whereas they had a focal localisation in Grape mutants (Fig. 5A,B and Supplementary Fig. 10A). The inhomogeneity of mitochondrion distribution was intermediate for Tangle and Bulb alleles and varied between the mutations (Fig. 5A,B and Supplementary Fig. 10A). When we plotted for each allele the mitochondrion distribution index to the locomotor performances and found a significant correlation (Fig. 5I). Hence, the more mitochondrion distribution is altered, the more a mutant is neurotoxic. We then investigated whether altering mitochondrion distribution affect the ER organisation and its interaction with mitochondria (Fig. 5C and Supplementary Fig. 10B). Unlike mitochondria, ER had a normal distribution in CMT2A motor neurons (Fig. 5D). Consistently, the asymmetric distribution between ER and mitochondria led to decreased level of ER signal overlapping mitochondria in the most toxic CMT2A alleles, including all Grape mutants, Tangle mutants *dL248V, dL92P* and *dH361Y* and Bulb mutants *dR364W* and *dK357N* (Fig. 5E). Grape mitochondria were less associated to the ER that was abnormally fragmented within mitochondrial clusters (Fig. 5F and Supplementary Fig. 10B). In contrast, the overlap of mitochondria with ER tubules was unchanged for Tangle and Bulb mutants and increased in Peanut mutants (Fig. 5F and Supplementary Fig. 10B). Because synaptic mitochondria are transported from the neuronal soma, we tested whether altered distribution in cell bodies could reduce mitochondrion content at neuromuscular junctions (NMJ). Most CMT2A alleles had decreased mitochondria at the NMJ, the most severe depletion being observed for the most toxic mutants (Fig. 5G, H and Supplementary Fig. 10C). Statistical analysis revealed that the

alterations of the relative ER-mitochondrion overlap and the depletion of NMJ mitochondria significantly correlated with the disturbance of mitochondrial distribution and with the level of locomotor deficit (Supplementary Table 1). In conclusion, the extent to which a given CMT2A allele is toxic in flies is proportional to the extent of which it alters mitochondria distribution.

Grape and Tangle alleles are insensitive to Parkin overexpression

Searching for genes whose overexpression could commonly rescue Grape, Tangle and Bulb mutants, we thought that increasing Mfn turnover could help neurons to cope with defective CMT2A proteins. In flies, MARF is targeted to degradation by the E3 ubiquitin ligase Parkin (Ziviani et al., 2010). Consistently, Parkin overexpression in *marfWT* controls increased fragmentation and reduced connectivity (Fig. 6A,B) whereas Parkin knockdown induced enlarged bulb-like mitochondria (Supplementary Fig. 11A). In contrast, Parkin overexpression in Grape and Tangle did not prevent mitochondrial clustering suggesting that the mutated proteins are resistant to Parkin-dependent degradation (Fig. 6A,B, Supplementary Fig. 11B,C). In Tangle, Parkin triggered a fragmentation of mitochondria that was stronger than the one observed in *marfWT* control (Fig. 6A,B, Supplementary Fig. 11C). This confirmed that the Tangle mutant are not active and suggested that the mitochondrial tubules found in Tangle mutants were generated by endogenous wild type MARF. Similarly, Parkin led to mitochondrial fragmentation in Peanut mutants (Fig. 6A,B, Supplementary Fig. 11D). Interestingly, Parkin induced mitochondrial clustering in *dR250Q* (Fig. 6A,B, Supplementary Fig. 11D). This phenotype possibly reflected a cryptic DN properties, revealed by the degradation of wild type but not *dR250Q* mutant proteins by Parkin. Consistent with these mitochondrial phenotypes, Parkin overexpression increased the developmental lethality in Grape, Tangle and Peanut mutants likely because Parkin target wild type but not mutant MARF (Fig. 6C). In contrast, Parkin overexpression lowered the occurrence of enlarged mitochondria in Bulb mutants (Fig. 6A,B and Supplementary Fig. 11E) and developmental lethality was not exacerbated by Parkin except for *dK357N* (Fig. 6C). Taken together, these observations demonstrated that most CMT2A mutations render MARF insensitive to Parkin.

Most CMT2A mutant have reduced ubiquitination and increased protein levels

These observations prompted us to investigate whether the CMT2A mutations interfered with MARF ubiquitination. Our transgenes driving HA-tagged MARF, we could specifically analysed these proteins independently of endogenous MARF. We first determine MARF ubiquitination profile in control *marfWT* flies. Anti-HA western blot against immuno-

precipitated MARF revealed three main bands at 100 kDa, 110 kDa and 130 kDa (Fig. 7A). Anti-Ubiquitin staining demonstrated that the 100 kDa band corresponds to native MARF whereas the 110 and 130 kDa bands were ubiquitinated forms (Fig 7A). Of note, a minor band with higher molecular weight and higher ubiquitination was also detected. Parkin was involved in the formation of the two main ubiquitinated forms of MARF as they both decreased upon *parkin* knockdown (Fig. 7B). We next determined the ratio between ubiquitinated and native MARF in our CMT2A allelic series. Ubiquitination was reduced in all CMT2A mutant proteins except for *dD214N* (Fig. 7C,D). Interestingly, the ubiquitination level of the mutant proteins correlated with the fusion capacity measured in knockout flies expressing the different CMT2A alleles (Supplementary Table 1). This ubiquitination defect was accompanied by increased levels of mutant MARF protein in most mutants (Fig. 7E) which correlated with decreased locomotor performance as well as focal distribution and clustering of mitochondria (Supplementary Table 1). Taken together, these data suggest that the CMT2A mutations affect MARF ubiquitination likely leading to mutant protein accumulation. This mechanism could potentiate the dominant properties of the CMT2A mutations.

Discussion

In vitro studies showed that Mfn2 dimerisation ability and GTPase activity is either decreased or increased depending on the CMT2A allele (Li et al., 2019). This suggested that these mutations could alter mitochondrial dynamics in different ways. We confirmed this in an *in vivo* context by comparing fourteen CMT2A alleles in drosophila. We defined four allelic classes affecting mitochondrial morphology in different manners and mitochondrial distribution to various extent. Notably, the more mitochondria had a focal distribution, the more locomotion was impaired in flies, and the more the disease was severe in patients.

We showed that the CMT2A mutations are enriched in specific Mfn2 regions, including many structures to which a molecular function was previously assigned. In the GTP-BD Ŭ2G, Ŭ3G and Ŭ4G helices, 44% of the a.a. are mutated in CMT2A. Although these helices only represent 6% of Mfn2, they account for 20% of all CMT2A alleles. Residues associated with Ŭ2G, Ŭ3G and Ŭ4G regions could be involved in dimerisation (Cao et al., 2017, Li et al., 2019) and interactions between domains (Beresewicz et al., 2018, Li et al., 2019). In the catalytic pocket, 30% of the residues forming the G1-4 motifs can be mutated. These loops form 6% of Mfn2 but concentrate 15% of CMT2A mutations. In HB1, mutations are more frequent along Ŭ3H1

and Ŭ4H1 in which 27.5% of the a.a. are mutated. These helices, that form the HR1/HR2 motives, represent 8% of Mfn2 and 18% of the CMT2A alleles. HR2 might be involved in transoligomerisation (Koshiba et al., 2004, Franco et al., 2016) while HR1 might negatively regulate HR2 function (Franco et al., 2016, Rocha et al., 2018) and destabilise lipid bilayers (Daste et al., 2018). Finally, the two flexible hinges supporting GTP-BD upward movement (Yan et al., 2018, Li et al., 2019) and HB1 ï HB2 closure (Low et al., 2009, De Vecchis et al., 2017) upon GTP hydrolysis are also impacted in CMT2A. It is striking that all the hinge 2 key residues, R94, R95, S332 and K357 (Yan et al., 2018, Li et al., 2019), are mutated in CMT2A. These observations have two implications. First, the hotspots that we defined could be used to improve Mfn2 mutation pathogenicity scoring, a novel variant having more chance to be pathogenic if it targets an a.a. from a hotspot. Second, the CMT2A hotspots could also be helpful to orient structure-function studies. Mutation hotspots highlight specific structures of interest and specific residues within these structures which analysis could improve our knowledge on Mfn molecular mechanism. In particular, the very high mutation frequency in Ŭ2G, Ŭ3G and Ŭ4G should stimulate in depth analysis of the role played by these structures in Mfn2 dynamics and oligomerisation.

Making hierarchical clustering of mitochondrial morphological parameters, we classified our CMT2A-mimetic alleles into four phenotypic classes: óGrapeô, óTangleô, óPeanutô and óBulbô. Regarding mitochondrial fusion capacity, Grape and Tangle alleles were inactive, Bulb mutants were active and Peanut mutant had residual activity. We could not correlate the Grape, Tangle, Peanut and Bulb alterations with specific domains or specific secondary structures targeted by the mutations. However, we found a correlation between the fusion activity of the mutants and the type of molecular consequences they were predicted to have on MARF. Mutants with no activity in *marfKO* affected the catalytic site (*dR104W*, *dH128R*, *dR259L*) and hydrophobic cores (*dL248V*, *dL92P*, *dH361Y*, *dL745P*) whereas mutants competent for fusion were at the interface between domains (*dD214N*, *dR250Q*, *dK357N*, *dR364W*) or at the molecular surface (*dW740S*).

Grape mutants act as strong DN with a high aggregative property, observed even in the absence of endogenous MARF. Hence, oligomerisation capacity was retained but fusion capacity was lost. Such phenomenon could occur because catalytic pocket mutants *dH128R* and *dR104W* would affect GTP hydrolysis, or because hinge 2 mutant *dR94W* would compromise conformational changes mediated by GTP hydrolysis. The fact that *dL248V* had a similar,

although milder, Grape phenotype could result from the alteration of the GTP-BD hydrophobic core in which L248 is implicated. In the absence of endogenous MARF, Tangle alleles had fragmented mitochondria that did not cluster. In contrast, in the presence of wild-type MARF, these alleles induced mitochondrial aggregation. However, unlike the Grape mutants, the Tangle alleles did not fully counteract the activity of wild-type MARF as mitochondria remained tubular. This suggests that the Tangle mutant proteins do not efficiently assemble with each other to form fusion complexes, but can more or less interact with wild-type MARF. In that case, the resulting fusion complexes might remain frozen at the docking step leading to clustering. Two Tangle mutants, *dL92P* and *dH361Y*, are part of a large hydrophobic network maintaining HB1 helices (Yan et al., 2018, Li et al., 2019), another one, *dR259L*, is part of G4 catalytic motif, and a third one, *dR400P*, is a HB2 surface residue. Interestingly, R259 in addition of being part of the catalytic pocket, as for R104 and H128, is involved in dimerisation through an interaction with E230 (Yan et al., 2018, Li et al., 2019). Hence the *dR259L* substitution by reducing the ability of mutant molecules to interfere with wild type ones could lead to a weaker DN phenotype than *dR104W* and *dH128R*. Peanut mutants had reduced fusion activity, *dR250Q*, that is at the GTP-BD ï HB1 interface being more active than *dL745P* that is part of HB1 hydrophobic core (Li et al., 2019). Finally, Bulb mutants contained enlarged bulb-shape mitochondria with normal ultrastructure that were typically described in fly and mammalian cells as a result of increased fusion or decreased fission (Wakabayashi et al., 2009, Rival et al., 2011, Kageyama et al., 2012, El Fissi et al., 2018). The Bulb alleles led to mitochondrial tubule formation in *marfKO* flies. Fusion-competent CMT2A alleles were first described in the landmark study of Detmer et al. in which four out of nine alleles were able to restore mitochondrial tubules in *Mfn1-Mfn2* double knockout cells (Detmer and Chan, 2007). Later, some CMT2A alleles were associated with excessive fusion in patient fibroblasts, HeLa cells and fly models (Codron et al., 2016, El Fissi et al., 2018, Das et al., 2022a, Das et al., 2022b, Das et al., 2024). Consistent with our result in flies, $Mfn2^{D214N}$ and $Mfn2^{W740S}$ were previously reported as fusion competent (Detmer and Chan, 2007, Li et al., 2019) whereas $Mfn2^{K357T}$ and $Mfn2^{R364W}$ were associated with enlarged mitochondria respectively in mouse and human cells (Stavropoulos et al., 2021, Das et al., 2022a, Das et al., 2024). The mechanism by which Bulb mutants lead to increased mitochondrial size is unknown and may differ between alleles as they target different protein regions: HB1ï HB2 interface for *dD214N*, GTP-BD ï HB1 and HB1 ï HB2 interfaces for *dR364W*, hinge 2 for *K357N* and HR2 surface for *W740S*. Recent studies suggested that complex mechanisms could be involved. The hyperfusion caused

by *Mfn2*^{R364W} in human cells being related to an inhibition of mitochondrial fission consecutive to the imbalance between Mfn2 and DRP1 ubiquitination (Das et al., 2022a, Das et al., 2022b).

Mfns from yeast, flies and mammals are the target of several E3 Ubiquitin ligases that regulate Mfn steady state level and Mfn-related functions in particular mitophagy (Escobar-Henriques and Joaquim, 2019, Alsayyah et al., 2020). In drosophila, Parkin ubiquitinates MARF and negatively regulates its expression level (Ziviani et al., 2010). When overexpressed in CMT2A flies, we observed that Parkin attenuated the phenotype of Bulb mutants but did not interfere with clustering in Grape and Tangle mutants. In Tangle mutants, mitochondria became more fragmented showing that the wild type molecules were efficiently targeted by Parkin. Regarding the Peanut class, Parkin induced mitochondrial clustering in *dR250Q* mutant suggesting that the degradation of wild type MARF revealed cryptic aggregative properties. The fact that Parkin is active on Bulb mutants that restores mitochondrial tubules formation in *marfKO* flies, but not on Grape, Tangle and Peanut alleles that are fusion-defective suggest a relation between MARF activity and Parkin-mediated ubiquitination. Interestingly, ubiquitination of Fzo1 and its subsequent degradation by the proteasome are required for the proper execution of the mitochondrial fusion process. Mutations in GTP-BD, including a CMT2A-related mutation, abolish Fzo1 ubiquitination and degradation by impairing Fzo1 interaction with the ubiquitin ligase SCF^{Mdm30} (Amiott et al., 2009, Anton et al., 2011, Cohen et al., 2011). Altered GTPase activity would indeed prevent a conformational change required to reveal an otherwise hidden C-ter binding site for SCF^{Mdm30} (Cohen et al., 2011). Interestingly, *mdm30* inactivation trigger an accumulation of Fzo1 that is paradoxically associated with the inhibition of mitochondrial fusion and the aggregation of mitochondria (Cohen et al., 2011). Because promoting Fzo1 degradation independently of SCF^{Mdm30} rescues this phenotype, it was proposed that Fzo1 turnover positively regulates mitochondrial fusion in yeast (Cohen et al., 2011). A similar mechanism could occur in flies and be affected by the CMT2A-associated mutations, possibly contributing to the mitochondrial clustering phenotype. Consistently, when we looked at the ubiquitination levels of mutant MARF by western blot, we found that ubiquitination was reduced in all loss-of-function mutants (*dR104W*, *dH128R*, *dDL92P*, *dR94W*, *dL248V*, *dH361Y*, *dL745P*). Although the overall decrease was lower, we also found reduced ubiquination in the mutants that restored mitochondrial tubulation in *marfKO* background (*dR250Q*, *dK357N*, *dR364W* and *dW740S* but not *dD214N*). This suggests that the *dR250Q*, *dK357N*, *dR364W* and *dW740S* mutations somehow perturb the functional interaction between MARF and Parkin when it is expressed at steady state level, this alteration being however compensated by Parkin

overexpression. Consistent with a role of ubiquitination in MARF turnover, we observed increased expression level in most CMT2A alleles. This observation suggest that defective ubiquitination increases the mutant to wild-type protein ratio possibly contributing to the dominant properties of the CMT2A alleles. However, although the most neurotoxic alleles were the most overexpressed (*dR104W*, *dH128R*, *dL92P*), the severity of the phenotype did not fully correlate with the expression levels in the all mutants. This demonstrates that the allele toxicity is primarily determined by its impact on Mfn activity, the alteration of expression level acting possibly as an amplifying mechanism.

In our CMT2A fly models, we observed varying degrees of neurotoxicity. Consistent with their phenotypes, the Grape alleles showed the highest toxicity in flies and Peanut the lowest. Tangle and Bulb mutants had intermediate toxicity which degree varied depending on the allele. Overall, we found that reduced locomotor performance correlated to the extent to which mitochondria had a focal distribution in neuronal cell bodies. The improper repartition of mitochondria in the cytoplasm could arise, depending on the mutant class, from aggregation and/or unbalanced fusion. This mitochondrial sequestration would presumably create dysfunction cytoplasmic regions by affecting the delivery of mitochondria to the areas where their activity is needed, in particular synapses, and by impairing the functional wiring of mitochondria to the rest of the organelle community. In addition, the abnormal Grape, Tangle and Bulb mitochondria were poorly connected to the network, possibly exacerbating the effects of their inefficient distribution. Importantly, phenotype severity in flies correlated well with disease severity in human. Grape mutants (*dR94W*, *dR104W*, *dH128R*, *dL248V*) as well as Tangle and Bulb mutants with the lower locomotion in flies (*dL92P*, *dH361Y*, *dR364W*, *dK357N*) corresponds to Mfn2 mutations causing severe and early onset forms of CMT2A (Kijima et al., 2005, Calvo et al., 2009, Stuppia et al., 2015). Conversely, the less affected Tangle (*dR259L*) and Bulb (*dD214N*, *dW740S*) mutants as well as the Peanut mutants (*dR250Q*, *dL745P*) correspond to Mfn2 mutations associated with mild and late onset forms of CMT2A (Nicholson et al., 2008, Ajroud-Driss et al., 2009, Nakhro, 2013, Stuppia et al., 2015). Of note, the observation we made in flies on *dR250Q* and *dD214N* strikingly echo the clinical data. Indeed, these two mutations which have a very weak phenotype in flies were both found in patients at the compound heterozygous state and proposed to act through a semi-dominant mechanism (Nicholson et al., 2008, Piscosquito et al., 2015, Tomaselli et al., 2016). Interestingly, in *dD214N* and *dR250Q*, as well as in *dW740S*, mutant flies MARF ubiquitination

was not altered. This should stimulate the search for correlation between Mfn2 ubiquitination status and disease severity in the perspective of improving disease prognosis for novel variants.

Taken together, our findings support the use of drosophila as a test tube to validate the implication of novel Mfn2 genetic variants in CMT2A and predict their putative severity. Overall, these data show a strong correlation between phenotype severity in flies and disease severity in human supporting the relevance of the drosophila model system in the study of CMT2A disease.

Methods

Protein sequence analysis and structure modelling

BLAST was used to retrieve the sequences of Mfns (MARF: 11 insect species ; MFN1 and MFN2: 11 vertebrate species) and of BDLPs (26 *Nostoc* species). BDLPs were aligned using T-Coffee (Notredame et al., 2000) simple alignment tool based on ClustalW. Mfns were aligned using the PSI-Coffee (Notredame et al., 2000). A.a. identity and similarity were calculated with SMS Ident and Sim (similarity groups: [G, A, V, L, I] ; [F, Y, W ; C, M ; S, T] ; [K, R, H] ; [D, E, N, Q] ; P). Outputs of these two alignments were merged using the T-Coffee Combine alignment algorithm. Mfn1, Mfn2, MARF and BDLP linear alignment was manually refined according to the structural alignment of Mfn2 (PDB: 6JFK) and BDLP (PDB: 2J68) (Low and Lowe, 2006, Li et al., 2019) obtained using ChimeraX (Goddard et al., 2018). Open and closed conformation BDLP structures (PDB: 2J68, 2W6D) (Low and Lowe, 2006, Low et al., 2009) were used as templates to build Mfn homology models. Because BDLP lacks the N-ter tail found in Mfns, we built N-ter truncated models of Mfn2 and MARF (Mfn2-ɑ1-23 and MARF-ɑ1-60). Transmembrane regions were predicted with TMpred (Cuthbertson et al., 2005). A single-template modelling script was used to generate over 100 of close- and open-conformation models using the MODELLER program (v 10.0) (Sali and Blundell, 1993). The GDP ligand was included to the catalytic pocket either by modelling procedure, or using ChimeraX (https://www.cgl.ucsf.edu/chimerax/). In the end, one homology model was selected based on the lowest *modpdb* value for the closed and open conformations of Mfn2 and MARF. The hydrogen were then added on a MolProbity (Chen et al., 2010). The stereochemical quality

was assessed using MolProbity and ProCheck. Z-score and local energy quality were determined using ProSA (Wiederstein and Sippl, 2007). Models of MARF dimers were generated using machine learning-based modelling (Jumper et al., 2021) with AlphaFold3 algorithm (https://alphafoldserver.com/). The resulting model was in a GDP-bound-like state (GTP-BD tilted upward) as found in resolved GDP-bound Mfn2 and Mfn1 truncated structures (Yan et al., 2018, Li et al., 2019). MARF with GTP-bound-like state (GTP-BD tilted downward) was generated with AlphaFold2, providing truncated Mfn1 GTP-bound structure (PDB: 5yew) as a template and reducing multiple alignment size (*max_msa*) (setting: 16:32) (https://colab.research.google.com/github/sokrypton/ColabFold/blob/main/AlphaFold2.ipyn). Graphical representation and residue mapping were generated using ChimeraX.

Drosophila stocks and culture

marf UAS lines: *marf* coding sequence was amplified from w^{1118} fly cDNAs and inserted into the pUASt-derived vector pPHW (from T. Murphy) by Gateway cloning using pDonr221 as intermediate. This *marf* sequence differed from the one on Flybase by silent mutations (natural polymorphisms and a synthetic EcoNI site introduced for screening convenience) (Supplementary sequence). *marf* 5ô and 3ô UTRs were not included. A CACC kozak sequence (Acevedo et al., 2018) and tree Nter HA tags were added. All CMT2A mutations were made by PCR (CloneAmp HIFI, Takara Bio). Constructs were verified by Sanger sequencing. Vectors carrying *marf* wild type or mutant alleles were inserted into chromosome 2L (25C6) by phiC31-mediated transgenesis using *w* ; *attP40* flies (Bestgene). Strains from BDSC: *elav-GAL4* (#458), *OK371-GAL4* (#26160), *UAS-myr::mRFP* (#7119), *UAS-KDEL::GFP* (#9898), *UAS-parkin_IR* (#38333, TRiP.HMS01800) and Y *3xP3-DsRed2* (#41459). The following lines were previously described by the authors: *UAS-mit::dendra2*, *marfKO* (El Fissi et al., 2018) and *UAS-mit::mKate2* (Poliacikova et al., 2023). *UAS-Parkin* was a generous gift from Ming Guo. GAL4/UAS fly crosses were grown at 29°C on a cornmeal-agar diet. We used third instar wandering larvae, except for *marfKO* larvae which stage could not be precisely determined as Mfn loss of function alters larval developmental (Sandoval et al., 2014, El Fissi et al., 2018).

Fly emergence quantification

elav-GAL4 / Y ; UAS-mit::dendra2 males were crossed to *UAS-marf*$^{CMT2A\ or\ WT}$ females providing a progeny in which females but not males expressed the CMT2A alleles.

Developmental lethality was assessed by counting the number of females and males in the adult offspring. On average, 125 individuals were scored in each condition.

Analysis of photoreceptor degeneration

elav-GAL4 UAS-marf$^{CMT2A\ or\ WT}$ *UAS-mit::dendra2* female flies were anesthetised with CO2 and decapitated with a micro-scissor. The back of the head was immediately glued with methyl cyanoacrylate onto a glass slide and the eyes covered with immersion oil (Leica Type F). Observations were made on a Zeiss Axioplan 2 microscope at 63X with light at maximum intensity and diaphragm at lower aperture. Photoreceptor degeneration was scored by counting the number of ommatidia with less than seven rhabdomeres. Per condition, we analysed on average 175 ommatidia from 8 individuals. Statistical analysis was performed using Mann-Whitney U test.

Locomotor assay

Fly development was carried out at 29°C, except for *dR94*, *dR104W*, and *dH128R* that were grown at 25°C to reduce developmental lethality and get adults. Adult flies (*elav-GAL4 ; UAS-marf*$^{CMT2A\ or\ WT}$ */ UAS-mit::dendra2*) were aged 10 days by group of 15 flies, the culture vials being changed every two days. Locomotor performance was determined by startled-induced negative geotaxis (SING). We used a culture vial in which one piece of PU foam plug was inserted at bottom and one at the top defining a free space of 65 mm height. Ten flies were introduced in the vial, allowed to recover from CO_2 anaesthesia (30 min) and tapped down to the bottom to trigger SING. A picture of the tube was taken 5 sec later using a digital camera. The height reached by each flies was measured using ImageJ. To test for the effect of vision on SING, a group of flies was first assessed into the complete darkness and then in the light. Tree independent races involving a total of 30 flies were performed per condition. Statistical analysis was performed using Mann-Whitney U test.

Live confocal imaging

Third instar larvae tissues were very rapidly dissected, mounted and observed under the microscope (<5 min). *marfKO* males were sorted thanks to a Y *3xP3mcherry* chromosome. CNS or ventral cuticle were mounted in PBS. Two bands of double face tape were placed on both side of the samples to avoid crushing between the coverslips and the slide. We imaged dorsal motor neuron clusters of the ventral nerve cords and NMJs located at the surface of muscles attached to the ventral cuticle. Z-image stacks (interval 0.2µm) covering the whole depth of motor neuron clusters or NMJs were acquired under a Zeiss LSM880 confocal

microscope at low laser intensity (<10%) with 63X (NMJs) or 100X (cell bodies) objectives. For high resolution observations, we used a Airyscan detector.

Mitochondrial morphology analysis

Airyscan-acquired Z-image stacks of living motor neurons (dorsal clusters of larval ventral nerve cord) expressing mit::dendra2 were submitted to deconvolution (Zen 2.3SP1 software with auto-settings). To analyse mitochondria in a wild type background, we used Z-stacks, Z-projection (Fiji, Temporal Colour Coder) and 3D reconstruction (Fiji, 3D project) as templates for scoring in blind pre-defined morphological mitochondrial traits i.e. fragmented, filamentous, enlarged, net-like and clustered. To quantify mitochondria length and connectivity in Peanut mutants and in *marfKO* flies, mitochondria were automatically segmented on confocal Z-projections of 10 images using a Weka classifier (Fiji, https://imagej.net/plugins/tws/) and total branch length and total branch number were determined using MitoAnalyser (Fiji https://github.com/AhsenChaudhry/Mitochondria-Analyzer) with default parameters.

Hierarchical clustering

First, we submitted to hierarchical clustering the quantifications of mitochondrion shape obtained when the CMT2A mutations are expressed in a wild type background. In these quantifications, the presence of 5 mitochondrial traits was scored in each cell analyzed (see above). Using the R package *stats* version 4.1.3, the distance matrix between each cell is calculated using the *dist* function with the *binary* method (as data is represented by the absence or presence of a mitochondrion trait). Then, a mean distance is calculated between each mutations. Then, the distance matrix between each mutation in a *marfKO* background is calculated for the mean mitochondrial length, for the percentage of fragmented mitochondrion (length below 0.6µ) and for the percentage of filamentous mitochondrion (length above 1.4µ) using the *dist* function with the *euclidean* method. Then, a hierarchical clustering between this new matrix and the previous matrix of mean distance of the presence/absence of the five mitochondrial traits is calculated using *hclustcompro* with the method *ward.D* from the R package *SPARTAAS* version 1.2.4 (https://CRAN.R-project.org/package=SPARTAAS), which is a tool allowing to combine distance matrices from two different sources to create this clustering and defined potential clusters. We let the tool calculate the alpha parameter, which is the mixing parameter giving different weights to each matrix. Here, it calculated an alpha of 0.59, giving more weight to the matrix between each mutation is calculated for the new

characters. Finally, the dendrogram created is also converted to newick format using the package *ape* version 5.7-1 (Paradis and Schliep, 2019) and visualized and the control sample set as the root of the dendrogram using SeaView version 5.0.5 (Gouy et al., 2021).

Electron Microscopy

Larval CNS were rapidly dissected, placed on a glass slide, incubated in a drop of fixation solution (FS) (2% paraformaldehyde, 2.5% glutaraldehyde, 5mM $CaCl_2$, 0.1mM Na Cacodylate) for 30 min at room temperature and embedded in a drop of 2% low melting agarose. Agarose cubes containing larval CNS were cut out with a scalpel and placed in FS for 24 hr at 4°C. This was followed by 2 hr post-fixation (2.5% glutaraldehyde, 0.8% Osmium tetroxide, 0.1mM Na Cacodylate) at 4°C. Ultrathin Epon plastic sections were contrasted in 2% uranyl acetate for 10 min and lead citrate for 2.5 min and observed with a Tecnai G2 TEM at 200 kv.

Mitochondrial content mixing

Dissected CNS from *OK371-GAL4, 2X[UAS-mit::dendra2]/UAS-HA::marf* larvae were observed under a Ropper-Nikon spinning disc confocal microscope equipped with photo-conversion module controlled by Metamorph. Mit::dendra2 was photoconverted at 450nm with 5% laser power for 1800 ms (300 iterations). Green (excitation 488nm) and red (excitation 545nm) mit::dendra2 signals were acquired repetitively during a time window of 180 sec. The photoconverted areas of the first image (area Ai) and last image (area Af) were measured using Fiji to calculate a diffusion index Af/Ai expressed as percent of control.

Mitochondrial and ER distribution

Confocal images of *OK371-GAL4, UAS-mit::dendra2/UAS-HA::marf ; UAS-myr::mRFP* 3rd instard larvae were cropped around individual motor neurons according the myr-mRFP signal and the size of all images adjusted to 128x128 pixel. The mit::dendra2 signal was automatically thresholded (Otsu method), and all pixel x and y coordinates were extracted. The variance of x and y coordinates was calculated and summed (x+y variance). For each condition, an average of nine cell bodies were analysed and the mean x+y variance was calculated and expressed as percent of control to obtain a mitochondrial distribution index. The same approach was used for ER distribution based on KDEL::GFP signal.

Mandersô correlation between ER and mitochondria staining

Confocal images of motor neuron of *OK371-GAL4, UAS-KDEL::GFP,UAS-mit::mKate2/UAS-HA::marf* 3rd instard larvae were automacally treated to remove background on each channel (Fiji, rolling ball method). Mandersô correlation coefficient between mit::mKate2 (mitochondria) and KDEL::GFP (ER) signals was then determined (Fiji, Coloc2 plugin).

NMJ mitochondrial content

NMJ Z-stacks were treated using Fiji to create Z-projections (maximum intensity) and perform an automatic threshold of the mit::dendra2 and myr::mRFP channels (Otsu method). The integrated pixel density, that is an expression of the area on binary images, was calculated for each bouton in each of the channel. The integrated density ratio, corresponding to ratio of the mitochondria area over the bouton area, was calculated. On average a hundred NMJ boutons were analysed in each condition.

Correlograms

Using the *cor* function from the R package stats version 4.1.3, we calculated the Kendall correlation coefficient between each quantitative variables. We choose the Kendall correlation coefficient over Pearson or Spearman because it is not parametric and avoid any assumptions about the data distribution. Then, these coefficients are plotted using the *corrplot* function from the R package *corrplot version 0.92* (https://github.com/taiyun/corrplot).

Code availability

The code used to generate the results is available in our Github repository **(**https://github.com/cedricmaurange/Varuk-et-al.git**)**

Antibodies for western blots

Primary antibodies: rabbit anti-Marf (gift from Alex Whitworth) (Ziviani et al., 2010) (1/1000), rat anti-HA (Roche, clone 3F10) (1/1000), rat anti-Ŭ-Tubulin (Abcam, Ab6160) (1/10.000), mouse anti-Ubiquitin (Merck, clone FK2) (1/500). Secondary HRP-coupled antibodies: rabbit anti-Rat (Jackson, 312-005-003), donkey anti-mouse (Jackson, 715-036-151), mouse anti-rabbit (Jackson, 211-032-171) (all at 1/20.000).

CNS protein extraction

Five third instar larva CNS were dissected, immediately immersed in 20µL of Laemmli buffer containing DTT and protease inhibitors (Complete, Roche), heated 20 min at 70°C, vigorously vortexed and stored at -20°C. Prior loading, protein samples were heated at 95°C for 5 min.

Immunoprecipitation

Twenty five 3rd instar larva CNS expressing HA::MARF were immersed in 100µl of cold lysis buffer (PBS, 0.1% NP40, Complete protease inhibitor from Roche and 1mm DTT) and frozen in liquid nitrogen. The operation was repeated tree times to obtain 75 CNS. The samples were rapidly thawed at 37°C and snap frozen in liquid nitrogen tree times, and then pooled and homogenized using a 1ml glass grinder and a tight Teflon pestle. The resulting suspension was centrifuged twice at 800 g and the supernatant frozen at -80°C before immuneprecipitation (IP). For IP, the sample was incubated 2 h at 4°C with rat anti-HA antibody (Roche, clone 3F10) (1/40). Protein G-coupled magnetic beads (Dynabeads, Thermo Fisher) were incubated for 45 min at 4°C with rabbit anti-rat antibody (Jackson, 312-005-003) (1/20) and then mixed with the HA-conjugated protein sample for 30 min at 4°C. The beads were washed according to manufacturer instructions and the immune-precipitated HA::MARF was recovered following a 10 min incubation at 95°C in Laemmli sample buffer containing fresh ϐ-mercaptoethanol.

Western Blotting

Proteins were separated on a 10% polyacrylamide gel in the presence of SDS at 100V. Transfer was done at 100V for 1.5 h either on nitrocellulose for larval CNS samples, or on Ethanol activated PVDF (0.45µ) for IP samples in 25mM Tris-Base, 190mM glycine supplemented with Ethanol (20% for nitrocellulose, 10% for PVDF). For anti-Ubiquitin staining on IP samples, PVDF membranes were boiled after transfer for 10 min in distilled water (Emmerich and Cohen, 2015). Blots were saturated in 5% BSA in PBS Tween20 0.05% (PBT), probed with primary antibody and corresponding HRP-coupled secondary antibodies with washing steps performed in PBT. Signal was revealed with chemiluminescent substrate (SuperSignal West Pico Plus for anti-HA and Atto for anti-Ubiquitin, Thermo Fisher) and images were acquired with a Bio-Rad imager. Blots of IP samples labelled with anti-Ubiquitin were stripped 7 min in Restore WB Stripping Buffer (Thermo Scientific), washed and relabelled with Anti-HA. Band pixel intensities were measured using ImageJ (gel analysis plugin) and quantification were performed on at least three independent blots with independent samples.

Acknowledgements

We deeply thank Jean-Pierre Duneau (LISM, Marseille) for sharing his expertise on protein structure *in silico* modelling and the members of IBDM microscopy and fly facilities for technical support. The IBDM-PiCsL imaging platform is supported by ANR investments for the future program (France-BioImaging, ANR-10-877 INSB-04-01). We are grateful to Alice Corbet, Elisa Montredon and Carole Rubio for their technical involvement. The experimental work expenses, the PhD fellowship of O. O. Varuk, the salaries of A. Ruiz and C. Rubio, and the internships of A. Corbet and C. Orengo were founded by the Association Française contre les Myopathies (AFM-téléthon) (research grant 22241 and 20097 to T. Rival and fellowship 22070 and 23855 to O. Varuk). We thank Lydia Kerkerian-Le Goff for her helpful scientific advices, and Laurent Kodjabachian and Pascale Durbec for supporting the completion of O. Varuk's PhD with IBDM funding. Stocks from the Bloomington Drosophila Stock Center were used in this study (NIH P40OD018537).

Figure Legends

Figure 1. Hotspots of CMT2A mutations in Mfn2.

A. Model of human Mfn2 structure predicted by homology modelling based on BDLP (a.a. 1-23 excluded). Spheres: carbon Ŭof the residues mutated in CMT2A.

B. Highlight on the GTP-BD (front view) from Mfn2 protein structure model.

C. Model of open Mfn2 structure (based on BDLP). Colour coding: proportion of a.a. mutated in CMT2A within a 10 a.a. interval. Arrows indicate the most affected secondary structures.

D. CMT2A mutation frequency in Mfn2 closed conformation (model based on BDLP).

E. CMT2A mutation frequency in Mfn2 GTP-BD (front view).

F. Model of Mfn2 open and closed conformations (based on BDLP) showing the residues mutated in CMT2A that were selected for our study in flies. The spheres represent the different atoms of the lateral chain (excluding hydrogen). Colour code refers to Mfn2 domains. Putative localisation of the selected CMT2A residues based on their lateral chain orientation and environment.

Figure 2. The CMT2A alleles differently alter mitochondrial shape and organisation.

A. Confocal Airyscan image Z-projections (20 slices) of mitochondrial networks (mit::dendra2) from living motor neurons (ventral nerve cord, dorsal clusters) of 3rd instar larva (*OK371-GAL4, UAS-mit::dendra2/UAS-HA::marf*^{WT} *or* ^{CMT2A}*)*. Colour code: Z-depth in dorso-ventral axis. Ø: flies with no *UAS-marf* transgene. *marfWT*: *UAS-HA::marf*^{WT}. Grape: *dR104W*. Tangle: *dL92P*. Bulb: *dK357N*. Peanut: *dL745P*. Arrows highlight mitochondrion morphological traits shown at higher magnification in the optic slices of bottom panel: tubular and fragmented (Ø and Peanut), net-like (*marfWT*), clustered and fragmented (Grape), clustered and filamentous (Tangle), enlarged (Bulb). TEM mitochondria high magnification views in motor neurons (dorsal clusters) from ventral nerve cord of 3rd instar larvae (*OK371-GAL4, UAS-mit::dendra2*).

B. Confocal Airyscan Z-projections (20 slices) of mitochondria (mit::dendra2) from motor neurons (ventral nerve cord, dorsal clusters) of *marfKO* male *marf* ^{ko}*/Y, 3xP3-mCherry* ; *OK371-GAL4, UAS-mit::dendra2/UAS-HA::marfWT or CMT2A* larvae. Grape: *dR104W*. Tangle: *dL92P*. Bulb: *dK357N*. Peanut: *dR250Q*. Colour code: Z-depth, dorso-ventral axis. Arrows: regions shown at high magnification in the bottom panels.

C. Photoconversion of mit::dendra2 (non-photoconverted in green and photoconverted in red) in living motor neurons (ventral nerve cord, dorsal clusters) from *OK371-GAL4, 2x UAS-*

mit::dendra2/UAS-marf 3rd instar larvae. Pictures show the first and last snap shots of a 3 min movie. White circle: position of the photoconvertion beam.

D. Mean diffusion index (ratio of final area containing photoconverted dendra2 over initial photoconverted area) as percent of the control (*marfWT*) +/- SD. Mann Whitney U test result: P<0.05/*, P<0.01/**, non-significant/ns.

Figure 3. Analysis of mitochondrial networks defined four CMT2A allelic groups.

A. Quantifications of mitochondrial morphology in larval motor neurons based on confocal Airyscan image analysis. A given cell can contain one or several morphological traits: fragmented, clustered, filamentous, net-like, enlarged. At least three individuals analysed per conditions. On average twelve motor neurons scored per conditions (minimum: seven cells).

B. Distribution of mitochondria (% of total mitochondria) in *marfKO* flies according to their length (µm). AL: average length (µm). At least 3 individuals analysed with an average total of 338 mitochondria (minimum: 167). Mann Whitney U test result versus $marf^{KO}$ P<0.05/*, P<0.001/***.

C. Dendrogram showing the results of the hierarchical clustering performed on the quantitative mitochondrial morphology in wild type (A) and *markKO* backgrounds (B). Hydrophobic core: a.a. lateral chain pointing toward the inside of the molecule and associated with a network of hydrophobic residues. Molecular surface: a.a. lateral chain pointing toward the exterior of the molecule. Domain interface: a.a. lateral chain in a given domain pointing toward another domain.

Figure 4. Varying degrees of neurotoxicity between the CMT2A alleles.

A. Hatching frequency of adult $UAS\text{-}marf^{WT}$ *or* ^{CMT2A} flies with or without *elav-GAL4* driver (average of 125 flies analysed per condition) ranked in each allelic group according to decreasing phenotypic strength. Dashed line: expected Mendelian frequency. ☺: moderate forms of CMT2A.

B. Average proportion of ommatidia containing less than seven visible photoreceptor rhabdomeres +/- SEM in the retina of one week old *elav-GAL4 ; UAS-mit::dendra2/UAS-HA::marfWT or CMT2A* adult flies ranked by allelic groups according to decreasing phenotypic strength. Images: ommatidia with seven (*elav>marfWT* fly) or less than seven (*elav>*$marf^{H128R}$ fly) photoreceptors. On average 175 ommatidia analysed from eight individuals per condition.

Mann Whitney U test result: P<0.05/*, P<0.01/**, P<0.001/***. ☺: moderate forms of CMT2A.

C. Average locomotor performance (startle-induced negative geotaxis) of ten days old *elav-GAL4 ; UAS-mit::dendra2/UAS-HA::marf*^{WT} *or* ^{CMT2A} adult flies. Histogram shows the proportion of flies according to the height they have reached (1: 0-15 mm, 2: >15-30 mm, 3: >30-45mm, 4: >45mm). Mean of three independent races involving a total of 30 flies. Mann Whitney U test result: P<0.05/*, P<0.01/**, P<0.001/***, non-significant/ns. ☺: moderate forms of CMT2A.

Figure 5. Alterations of mitochondrial distribution correlates with neurotoxicity.

A. Confocal microscopy of living motor neurons showing mitochondria and plasma membrane in *OK371-GAL4, UAS-mit::dendra2 ; UAS-myr::mRFP* 3rd instar larva overexpressing control (*marfWT*) and *dL92P marf (marf*^{CMT2A}).

B. Mean mitochondrial distribution index +/- SD. Variance of all mitochondrial pixel coordinates (x,y) was analysed on average on nine cell bodies. Mann Whitney U test result: P<0.05/*, P<0.01/**, P<0.001/***.

C. Confocal Airyscan microscopy images of living motor neurons showing mitochondria and ER in *OK371-GAL4, UAS-mit::kate2, UAS-KDEL::GFP* 3rd instar larva overexpressing control (*UAS-marf*^{WT}) or *dL92 marf (UAS-marf*^{CMT2A}). Magnification views: ER and mitochondria in close vicinity and overlapping (arrow heads).

D. Mean distribution index of endoplasmic reticulum for the different CMT2A alleles +/- SD. At least, tree cell bodies analysed per condition. Mann Whitney U test result: not significant.

E. Histogram showing mean Manderôs coefficient (percent of *marfWT*) representing the fraction of KDEL::GFP (ER) signal overlapping with mit::mKate2 (mitochondria) staining +/- SD (sum of GFP pixel intensities with mKate2 intensity above 0 divided by the total GFP pixel intensity). Average image number analysed: 19 (minimum 14). U test result: P<0.05/*, P<0.01/**, P<0.001/***.

F. Mean Manderôs coefficients (percent of *marfWT*) representing the fraction of mit::mKate2 (mitochondria) signal overlapping with KDEL::GFP (ER) staining +/- SD (sum of mKate2 pixel intensities with GFP intensity above 0 divided by the total mKate2 pixel intensity). Average image number analysed: 19 (minimum 14). U test result: P<0.05/*, P<0.01/**, P<0.001/***.

G. Confocal Airyscan microscopy images showing mitochondria within NMJ boutons in living muscles from *OK371-GAL4, UAS-mit::dendra2 ; UAS-myr::mRFP* 3rd instar larva overexpressing wild type *marf* (*UAS-marf*^{WT}) or *dL92P* mutant *marf* (*marf*^{CMT2A}). Insight: high magnification view of synaptic boutons.

H. Mean ratio of mitochondrial over bouton area +/- SD. Average boutons analysed:100). U test result: P<0.05/*, P<0.01/**, P<0.001/***.

I. Correlation plot between mitochondrial distribution in motor neuron soma (data Fig. 5A) and locomotor performances (data Fig. 4C) both expressed as percent of control (*marfWT*). Ű Kendall correlation coefficient. p: p-value.

Figure 6. Most CMT2A alleles are insensitive to Parkin overexpression.

A. Confocal Airyscan images from living motor neuron of *OK371-GAL4, UAS-mit::dendra2/UAS-HA::marf*^{WT} *or* ^{CMT2A}*, UAS-parkin* 3rd instar larva overexpressing Parkin (*parkin*^{OE}). The mitochondrial structures pinpointed by arrows are magnified on bottom panel images. Grape: *dR94W*. Tangle: *dL92P*. Peanut: *dL745P*. Bulb: *dR364W*.

B. Quantifications of mitochondrial morphology in larval motor neurons overexpressing Parkin (*parkin*^{OE}) based on confocal Airyscan image stacks. A given cell can contain mitochondria with one or several morphological traits: fragmented, clustered, filamentous, net-like, enlarged. Black lines: phenotypes without Parkin overexpression. Red surfaces: phenotype upon Parkin overexpression. At least three individual were analysed. Average total number of motor neurons analysed: 11 (minimum 6).

C. Lethality in CMT2A flies with (+) or without (-) *parkin* overexpression (*parkin*^{OE}). Males *elav-GAL4/Y ; UAS-mit::dendra2* flies were crossed to females *UAS-marf*^{WT} or ^{CMT2A}. In the resulting adult progeny, the number of males (no *elav-GAL4,* no *UAS-marf*^{WT} or ^{CMT2A} expression) and females (*with elav-GAL4,* with *marf*^{WT} or ^{CMT2A} expression) was determined to calculate the difference in percent between the males and females populations referred as percent survival. The percent lethality correspond to 100 minus the percent survival.

Figure 7. Decreased ubiquitination and increased protein level in CMT2A mutant MARF.

A. Anti-HA and anti-Ubiquitin western blot analysis of immunoprecipitated wild type HA-tagged MARF (IP) from *elav-GAL4 ; UAS-mit::dendra2/UAS-HA::marf*^{WT} 3rd instar larva CNS. Input corresponds to the protein extract before IP. The same blot was first stained with anti-Ubiquitin, and following stripping, was re-probed with anti-HA. Black arrows: ubiquitinated MARF.

B. Anti-HA western blot analysis of protein extracts from *elav-GAL4 ; UAS-mit::dendra2/UAS-HA::marf*^{WT} larval CNS alone or with *UAS-RNAi* against *parkin* (*parkin*^{KD}). Black arrows: ubiquitinated MARF.

C. Anti-HA and anti-Ŭ-Tubulin western blot analysis of protein extracts from CNS of *elav-GAL4 ; UAS-mit::dendra2/UAS-HA::marf*^{WT} or ^{CMT2A} larvae. Black arrows: ubiquitinated MARF. White arrow: native MARF.

D. Average ratio between ubiquitinated and native MARF based on western blot signal intensity analysis. Mean +/- SD of 3 experiments each independent sample involving 5 CNS. Mann Whitney U test result: P<0.05/*, P<0.01/**.

E. Average native MARF level (arbitrary units) based on western signal intensity (Ŭ-tubulin used for normalisation). Mean +/- SD of 3 experiments each independent sample involving 5 CNS. Mann Whitney U test result: P<0.05/*, P<0.01/**.

Supplementary figure and table legends

Fig. S1. Secondary structures targeted by CMT2A mutation hotspots.

A. Frequency of the CMT2A mutation along the a.a. sequence of human Mfn2 showing hotspots of mutations in specific secondary structures. Heat map correspond to the proportion of mutated a.a. within a specific secondary structure.

B. Resolved structure of human Mfn1 dimers (Yan et al., 2018) in the GTP-bound/open (PDB: 5yew) (top and right panels) and the GDP-bound/close (PDB: 5gom) (bottom panel). To superimpose the CMT2A mutation heat map shown Fig. 1 on Mfn1 structures, Mfn1 and Mfn2 sequences were aligned and the frequency of mutations for a given 10 a.a. interval of Mfn2 was assigned to the homologous interval in Mfn1. Arrows indicate the most affected secondary structures.

Fig. S2. Most amino acids mutated in CMT2A are conserved in MARF.

A. Alignment of a.a. sequences from human Mfn1 and Mfn2 (UniProt: Q8IWA4 and O95140) (hMfn1 and hMfn2) and *D. melanogaster* MARF (UniPrto: Q7YU24) (dMARF). Black: identical residues between MARF and/or Mfn1 and Mfn2 sequences. Dark pink in Mfn2: residues mutated in CMT2A. Dark pink in MARF: residues identical to CMT2A-involved a.a.. Pale pink in MARF: residues with physicochemical properties similar to CMT2A-involved ones. Red frames: G1, G2, G3, G4 motifs. In G2, Mfn2-T129, MARF-T170 and Mfn1-I108 are highlighted in blue. Black frames: HR1 and HR2 motifs. HB1 and GTP-BD Ŭ-helices are shown as cylinders and GTP-BD ɓ-strands as arrows following Mfn2 truncated structure (PDB: 6JFK) (Li et al., 2019). HB2 Ŭ helices are predicted from BDLP and TM from TMpred. Numbers corresponds to the positions of CMT2A a.a. substitutions, the ones that have been coloured being selected for investigation in drosophila.

B. Percentage of identity and similarity between the sequences from drosophila MARF (Q7YU24), human Mfn2 (O95140) (considering all a.a. or only those mutated in CMT2A) and human Mfn1 (Q8IWA4).

C. Positions of the CMT2A-related residues selected for our study in flies in the sequence of Mfn2, MARF and Mfn1 based on sequence alignment.

Fig. S3. Models of MARF protein structures

A. Model of MARF structure (a.a. 1- 60 deleted) predicted by homology modelling based on BDLP GTP-bound/open conformation. Spheres correspond to the lateral chain atoms (except hydrogens) of a.a. that have been mutated in flies to mimic CMT2A alleles.

B. Model of MARF structure (a.a. 1- 60 deleted) predicted by homology modelling based on BDLP GDP-bound/close conformation. Spheres correspond to the lateral chain atoms (except hydrogens) of a.a. that have been mutated in flies to mimic CMT2A alleles.

C. MARF BDLP-based model. Highlight on GTP-BD and HB1 interface (side view). Sticks: a.a. lateral chains.

D. MARF BDLP-based model. Highlight on GTP-BD catalytic site (front view). Sticks: a.a. lateral chains.

E. MARF BDLP-based model. Highlight on HB1 (top view). Sticks: a.a. lateral chains.

F. Model of MARF dimer structure (a.a. 1- 60 deleted) predicted by machine learning-based modelling (AlphaFold3). Spheres: lateral chain atoms (except hydrogens) of a.a. that have been mutated in flies to mimic CMT2A alleles. Top panel: side view. Bottom panel: top view.

Fig. S4. Comparison of CMT2A-related residues lateral chain localisation and orientation in MARF models and resolved structures of Mfn2 and Mfn1.

A. Front view of the catalytic site in AlphaFold3 MARF model and resolved structure of Mfn2.

B. Top view of the dimer interface formed by GTP-BD in AlphaFold3 MARF model and resolved structure of Mfn1.

C. Side view of GTP-BD and HB1 in AlphaFold3 MARF model and resolved structure of Mfn2 GDP-bound state.

D. Side view of GTP-BD and HB1 in AlphaFold3 MARF model generated using an Mfn1 GTP-bound template and resolved structure of Mfn1 GTP-bound.

E. Top view of HB1 in AlphaFold3 MARF model and resolved structure of Mfn2 GDP-bound.

F. Bottom view of the GTP-BD in AlphaFold3 MARF model and resolved structure of Mfn2 GDP-bound.

Fig. S5. Neuronal overexpression of HA-tagged MARF in larval CNS.

A. Scheme of the UAS/GAL4 system used to express wild type and CMT2A mutant forms of HA-tagged MARF in all neurons (*elav-GAL4*) or in motor neurons (*OK371-GAL4*).

B. Anti-MARF and anti-Ŭ-tubulin western blot analysis of larval CNS protein extracts from *marfKO*, control flies expressing only endogenous MARF (white arrow) and *elav-GAL4, UAS-HA::marf* flies overexpressing HA::MARF (black arrow).

C. Fold protein expression of HA-tagged MARF relative to endogenous MARF. Mean of 6 independent samples +/- SD.

Fig. S6. Mitochondrial phenotypes associated with the CMT2A mutations in a wild type background.

Confocal Airyscan image Z-projections (20 slices) of mitochondrial networks (mit::dendra2) from living motor neuron (dorsal clusters of ventral nerve cord) of *OK371-GAL4, UAS-mit::dendra2/UAS-HA::marf*^{WT} *or* ^{CMT2A} 3rd instar larvae. Colour code: Z-depth in dorso-ventral axis. Intermediate panels: high magnification optic slices of mitochondria structures pinpointed by arrows on upper panels. Bottom panels: TEM mitochondria high magnification views in motor neurons (dorsal clusters) from larval ventral nerve cords.

A. Ø: wild type (no *marf* transgene). *marfWT* (*UAS-HA::marf*^{WT}).

B. Grape alleles (*UAS-HA::marf*^{CMT2A}).

C. Tangle alleles (*UAS-HA::marf*^{CMT2A}).

D. Bulb alleles (*UAS-HA::marf*^{CMT2A}).

E. Peanut alleles (*UAS-HA::marf*^{CMT2A}).

Fig. S7. Mitochondrial phenotypes associated with the CMT2A mutations in a *marfKO* background.

Confocal Airyscan image Z-projections (20 slices) of mitochondrial networks (mit::dendra2) from living motor neuron (dorsal clusters of ventral nerve cord) of male *marf* ^{KO}*/Y, 3xP3-mCherry* ; *OK371-GAL4, UAS-mit::dendra2/UAS-HA::marf*^{WT} *or* ^{CMT2A} 3rd instar larvae. Colour code: Z-depth in dorso-ventral axis. Intermediate panels: high magnification optic slices of mitochondria structures pinpointed by arrows on upper panels. Bottom panels: TEM mitochondria high magnification views in motor neurons (dorsal clusters) from larval ventral nerve cords.

A. Ø: no *marf* transgene. *marfWT* (*UAS-HA::marf*^{WT}).

B. Grape alleles (*UAS-HA::marf*^{CMT2A}).

C. Tangle alleles (*UAS-HA::marf*^{CMT2A}).

D. Bulb alleles (*UAS-HA::marf*^{CMT2A}).

E. Peanut alleles (*UAS-HA::marf*^{CMT2A}).

Fig. S8. Mitochondrial morphology in Peanut mutants.

Quantification of mitochondrial morphology in mit::dendra2-labelled motor neurons from larvae expressing only endogenous *marf* (*control*), overexpressing wild type *marf* (*UAS-marf*^{WT}) or Peanut *marf* mutant *dR250Q* and *dL745P*.

A. Mean mitochondrial length +/- SD. Mann Whitney U test result: versus control P<0.05/*, P<0.001/***, versus *marfWT* P<0.001/$^{###}$

B. Mean mitochondrial connectivity +/- SD (number of branches). Mann Whitney U test result: versus control P<0.001/***, versus *marfWT* P<0.001/$^{###}$

C. Distribution of mitochondria according to their length.

D. Distribution of mitochondria according to their number of branches.

Fig. S9. Startled-induced locomotion does not require vision.

Average locomotor performance (startle-induced negative geotaxis) of 10 days old *elav-GAL4 ; UAS-mit::dendra2/+*adult flies placed in the dark or in the light. Histogram shows the proportion of flies according to the height they have reached (1: 0-15 mm, 2: >15-30 mm, dark 3: >30-45mm, 4: >45mm). Mean of three independent races each involving 10 flies.

Fig. S10. Impact of the CMT2A alleles on mitochondrion distribution, relative ER-mitochondrion localisation and mitochondrion NMJ content.

A. Confocal microscopy images of living motor neurons in *OK371-GAL4, UAS-mit::dendra2 ; UAS-myr::mRFP* 3rd instar larva showing mitochondria and plasma membrane overexpressing wild type (*marfWT*) or CMT2A mutant *marf* from the four allelic groups.

B. Confocal Airyscan microscopy images of living motor neurons showing mitochondria and ER in *OK371-GAL4, UAS-mit::kate2, UAS-KDEL::GFP* 3rd instar larva overexpressing control (*marfWT*) and *CMT2A* mutant *marf* from the four allelic groups. Magnification views: ER and mitochondria in close vicinity and overlapping (arrow heads).

C. Confocal Airyscan microscopy images showing mitochondria within NMJ boutons at the surface of living muscles from *OK371-GAL4, UAS-mit::dendra2/UAS-HA::marf ; UAS-myr::mRFP* 3rd instar larva overexpressing wild type (*mar*^{fWT}) or ^{CMT2A} mutant *marf* from the four allelic groups.

Fig. S11. Parkin overexpression in CMT2A mutants.

Confocal Airyscan image Z-projections (20 slices) of mitochondrial networks (mit::dendra2) from living motor neuron (dorsal clusters of ventral nerve cord) of control and CMT2A mutant

OK371-GAL4, UAS-mit::dendra2 / /UAS-HA::marf^{WT} *or* ^{CMT2A}*, UAS-parkin* 3rd instar larva overexpressing *parkin*. Colour code: Z-depth in dorso-ventral axis. Intermediate panels: high magnification optic slices of mitochondria structures pinpointed by arrows on upper panels. Bottom panels: TEM mitochondria high magnification views in motor neurons (dorsal clusters) from larval ventral nerve cords.

A. *marfWT*: overexpression of wild type *marf* (*UAS-HA::marf*^{WT}). *marfWT* + *parkin*^{OE}: overexpression of wild type *marf* and *parkin* (*UAS-HA::marf*^{WT}*, UAS-parkin*). *marfWT* + *parkin*^{KD}: overexpression of wild type *marf* and knockdown of *parkin* (*UAS-HA::marf*^{WT} ; *UAS-parkin RNAi*).

B. Grape alleles with overexpression of *parkin* (*UAS-HA::marf*^{Grape}*, UAS-parkin*).

C. Tangle alleles with overexpression of *parkin* (*UAS-HA::marf*^{Tangle}*, UAS-parkin*).

D. Bulb alleles with overexpression of *parkin* (*UAS-HA::marf*^{Bulb}*, UAS-parkin*).

E. Peanut alleles with overexpression of *parkin* (*UAS-HA::marf*^{Peanut}*, UAS-parkin*).

Supplementary Table 1. Correlation plots.

A. Correlogram showing Kendall coefficient (Ű) between the indicated variables.

B. P-value corresponding to the level of significance of the correlations presented in A.

References

Acevedo JM, Hoermann B, Schlimbach T, Teleman AA (2018) Changes in global translation elongation or initiation rates shape the proteome via the Kozak sequence. Scientific reports 8:4018.

Ajroud-Driss S, Fecto F, Ajroud K, Yang Y, Donkervoort S, Siddique N, Siddique T (2009) A novel de novo MFN2 mutation causing CMT2A with upper motor neuron signs. Neurogenetics 10:359-361.

Alsayyah C, Ozturk O, Cavellini L, Belgareh-Touze N, Cohen MM (2020) The regulation of mitochondrial homeostasis by the ubiquitin proteasome system. Biochim Biophys Acta Bioenerg 1861:148302.

Alsayyah C, Singh MK, Morcillo-Parra MA, Cavellini L, Shai N, Schmitt C, Schuldiner M, Zalckvar E, Mallet A, Belgareh-Touze N, Zimmer C, Cohen MM (2024) Mitofusin-mediated contacts between mitochondria and peroxisomes regulate mitochondrial fusion. PLoS Biol 22:e3002602.

Amiott EA, Cohen MM, Saint-Georges Y, Weissman AM, Shaw JM (2009) A mutation associated with CMT2A neuropathy causes defects in Fzo1 GTP hydrolysis, ubiquitylation, and protein turnover. Molecular biology of the cell 20:5026-5035.

Anton F, Fres JM, Schauss A, Pinson B, Praefcke GJ, Langer T, Escobar-Henriques M (2011) Ugo1 and Mdm30 act sequentially during Fzo1-mediated mitochondrial outer membrane fusion. Journal of cell science 124:1126-1135.

Beresewicz M, Charzewski L, Krzysko KA, Kochanski A, Zablocka B (2018) Molecular modelling of mitofusin 2 for a prediction for Charcot-Marie-Tooth 2A clinical severity. Scientific reports 8:16900.

Bertholet AM, Delerue T, Millet AM, Moulis MF, David C, Daloyau M, Arnaune-Pelloquin L, Davezac N, Mils V, Miquel MC, Rojo M, Belenguer P (2016) Mitochondrial fusion/fission dynamics in neurodegeneration and neuronal plasticity. Neurobiology of disease 90:3-19.

Brandner A, De Vecchis D, Baaden M, Cohen MM, Taly A (2019) Physics-based oligomeric models of the yeast mitofusin Fzo1 at the molecular scale in the context of membrane docking. Mitochondrion 49:234-244.

Brandt T, Cavellini L, Kuhlbrandt W, Cohen MM (2016) A mitofusin-dependent docking ring complex triggers mitochondrial fusion in vitro. Elife 5.

Calvo J, Funalot B, Ouvrier RA, Lazaro L, Toutain A, De Mas P, Bouche P, Gilbert-Dussardier B, Arne-Bes MC, Carriere JP, Journel H, Minot-Myhie MC, Guillou C, Ghorab K, Magy L, Sturtz F, Vallat JM, Magdelaine C (2009) Genotype-phenotype correlations in Charcot-Marie-Tooth disease type 2 caused by mitofusin 2 mutations. Archives of neurology 66:1511-1516.

Cao YL, Meng S, Chen Y, Feng JX, Gu DD, Yu B, Li YJ, Yang JY, Liao S, Chan DC, Gao S (2017) MFN1 structures reveal nucleotide-triggered dimerization critical for mitochondrial fusion. Nature 542:372-376.

Cartoni R, Martinou JC (2009) Role of mitofusin 2 mutations in the physiopathology of Charcot-Marie-Tooth disease type 2A. Experimental neurology 218:268-273.

Chen H, Chomyn A, Chan DC (2005) Disruption of fusion results in mitochondrial heterogeneity and dysfunction. The Journal of biological chemistry 280:26185-26192.

Chen VB, Arendall WB, 3rd, Headd JJ, Keedy DA, Immormino RM, Kapral GJ, Murray LW, Richardson JS, Richardson DC (2010) MolProbity: all-atom structure validation for macromolecular crystallography. Acta Crystallogr D Biol Crystallogr 66:12-21.

Codron P, Chevrollier A, Kane MS, Echaniz-Laguna A, Latour P, Reynier P, Bonneau D, Verny C, Procaccio V, Lenaers G, Cassereau J (2016) Increased mitochondrial fusion in a autosomal recessive CMT2A family with mitochondrial GTPase mitofusin 2 mutations. Journal of the peripheral nervous system : JPNS 21:365-369.

Cohen MM, Amiott EA, Day AR, Leboucher GP, Pryce EN, Glickman MH, McCaffery JM, Shaw JM, Weissman AM (2011) Sequential requirements for the GTPase domain of the mitofusin Fzo1

and the ubiquitin ligase SCFMdm30 in mitochondrial outer membrane fusion. Journal of cell science 124:1403-1410.
Cohen MM, Leboucher GP, Livnat-Levanon N, Glickman MH, Weissman AM (2008) Ubiquitin-proteasome-dependent degradation of a mitofusin, a critical regulator of mitochondrial fusion. Molecular biology of the cell 19:2457-2464.
Cuthbertson JM, Doyle DA, Sansom MS (2005) Transmembrane helix prediction: a comparative evaluation and analysis. Protein Eng Des Sel 18:295-308.
Das R, Das S, Chakrabarti S, Chakrabarti O (2022a) CMT2A-linked mitochondrial hyperfusion-driving mutant MFN2 perturbs ER-mitochondrial associations and Ca(2+) homeostasis. Biol Cell 114:309-319.
Das R, Kamal IM, Das S, Chakrabarti S, Chakrabarti O (2022b) MITOL-mediated DRP1 ubiquitylation and degradation promotes mitochondrial hyperfusion in a CMT2A-linked MFN2 mutant. Journal of cell science 135.
Das R, Maity S, Das P, Kamal IM, Chakrabarti S, Chakrabarti O (2024) CMT2A-linked MFN2 mutation, T206I promotes mitochondrial hyperfusion and predisposes cells towards mitophagy. Mitochondrion 74:101825.
Daste F, Sauvanet C, Bavdek A, Baye J, Pierre F, Le Borgne R, David C, Rojo M, Fuchs P, Tareste D (2018) The heptad repeat domain 1 of Mitofusin has membrane destabilization function in mitochondrial fusion. EMBO reports 19.
De Vecchis D, Brandner A, Baaden M, Cohen MM, Taly A (2019) A Molecular Perspective on Mitochondrial Membrane Fusion: From the Key Players to Oligomerization and Tethering of Mitofusin. J Membr Biol 252:293-306.
De Vecchis D, Cavellini L, Baaden M, Henin J, Cohen MM, Taly A (2017) A membrane-inserted structural model of the yeast mitofusin Fzo1. Scientific reports 7:10217.
Debattisti V, Pendin D, Ziviani E, Daga A, Scorrano L (2014) Reduction of endoplasmic reticulum stress attenuates the defects caused by Drosophila mitofusin depletion. The Journal of cell biology 204:303-312.
Detmer SA, Chan DC (2007) Complementation between mouse Mfn1 and Mfn2 protects mitochondrial fusion defects caused by CMT2A disease mutations. The Journal of cell biology 176:405-414.
El Fissi N, Rojo M, Aouane A, Karatas E, Poliacikova G, David C, Royet J, Rival T (2018) Mitofusin gain and loss of function drive pathogenesis in Drosophila models of CMT2A neuropathy. EMBO reports.
Emmerich CH, Cohen P (2015) Optimising methods for the preservation, capture and identification of ubiquitin chains and ubiquitylated proteins by immunoblotting. Biochemical and biophysical research communications 466:1-14.
Escobar-Henriques M, Joaquim M (2019) Mitofusins: Disease Gatekeepers and Hubs in Mitochondrial Quality Control by E3 Ligases. Front Physiol 10:517.
Formosa LE, Ryan MT (2016) Mitochondrial fusion: Reaching the end of mitofusin's tether. The Journal of cell biology 215:597-598.
Franco A, Kitsis RN, Fleischer JA, Gavathiotis E, Kornfeld OS, Gong G, Biris N, Benz A, Qvit N, Donnelly SK, Chen Y, Mennerick S, Hodgson L, Mochly-Rosen D, Dorn GW, II (2016) Correcting mitochondrial fusion by manipulating mitofusin conformations. Nature 540:74-79.
Giacomello M, Pyakurel A, Glytsou C, Scorrano L (2020) The cell biology of mitochondrial membrane dynamics. Nature reviews Molecular cell biology 21:204-224.
Goddard TD, Huang CC, Meng EC, Pettersen EF, Couch GS, Morris JH, Ferrin TE (2018) UCSF ChimeraX: Meeting modern challenges in visualization and analysis. Protein Sci 27:14-25.
Gordaliza-Alaguero I, Canto C, Zorzano A (2019) Metabolic implications of organelle-mitochondria communication. EMBO reports 20:e47928.
Gouy M, Tannier E, Comte N, Parsons DP (2021) Seaview Version 5: A Multiplatform Software for Multiple Sequence Alignment, Molecular Phylogenetic Analyses, and Tree Reconciliation. Methods Mol Biol 2231:241-260.

Hwa JJ, Hiller MA, Fuller MT, Santel A (2002) Differential expression of the Drosophila mitofusin genes fuzzy onions (fzo) and dmfn. Mechanisms of development 116:213-216.
Jumper J, Evans R, Pritzel A, Green T, Figurnov M, Ronneberger O, Tunyasuvunakool K, Bates R, Zidek A, Potapenko A, Bridgland A, Meyer C, Kohl SAA, Ballard AJ, Cowie A, Romera-Paredes B, Nikolov S, Jain R, Adler J, Back T, Petersen S, Reiman D, Clancy E, Zielinski M, Steinegger M, Pacholska M, Berghammer T, Bodenstein S, Silver D, Vinyals O, Senior AW, Kavukcuoglu K, Kohli P, Hassabis D (2021) Highly accurate protein structure prediction with AlphaFold. Nature 596:583-589.
Kageyama Y, Zhang Z, Roda R, Fukaya M, Wakabayashi J, Wakabayashi N, Kensler TW, Reddy PH, Iijima M, Sesaki H (2012) Mitochondrial division ensures the survival of postmitotic neurons by suppressing oxidative damage. The Journal of cell biology 197:535-551.
Kijima K, Numakura C, Izumino H, Umetsu K, Nezu A, Shiiki T, Ogawa M, Ishizaki Y, Kitamura T, Shozawa Y, Hayasaka K (2005) Mitochondrial GTPase mitofusin 2 mutation in Charcot-Marie-Tooth neuropathy type 2A. Hum Genet 116:23-27.
Koshiba T, Detmer SA, Kaiser JT, Chen H, McCaffery JM, Chan DC (2004) Structural basis of mitochondrial tethering by mitofusin complexes. Science 305:858-862.
Li YJ, Cao YL, Feng JX, Qi Y, Meng S, Yang JF, Zhong YT, Kang S, Chen X, Lan L, Luo L, Yu B, Chen S, Chan DC, Hu J, Gao S (2019) Structural insights of human mitofusin-2 into mitochondrial fusion and CMT2A onset. Nat Commun 10:4914.
Low HH, Lowe J (2006) A bacterial dynamin-like protein. Nature 444:766-769.
Low HH, Sachse C, Amos LA, Lowe J (2009) Structure of a bacterial dynamin-like protein lipid tube provides a mechanism for assembly and membrane curving. Cell 139:1342-1352.
Nakhro KP, J.M. Choi, B.O. Chung, K.W. (2013) Missense mutations ofmitofusin 2in axonal CharcotMarieTooth neuropathy: polymorphic orincomplete penetration? Animal Cells and Systems Vol. 17: 228-236.
Nicholson GA, Magdelaine C, Zhu D, Grew S, Ryan MM, Sturtz F, Vallat JM, Ouvrier RA (2008) Severe early-onset axonal neuropathy with homozygous and compound heterozygous MFN2 mutations. Neurology 70:1678-1681.
Notredame C, Higgins DG, Heringa J (2000) T-Coffee: A novel method for fast and accurate multiple sequence alignment. J Mol Biol 302:205-217.
Ono T, Isobe K, Nakada K, Hayashi JI (2001) Human cells are protected from mitochondrial dysfunction by complementation of DNA products in fused mitochondria. Nature genetics 28:272-275.
Paradis E, Schliep K (2019) ape 5.0: an environment for modern phylogenetics and evolutionary analyses in R. Bioinformatics 35:526-528.
Pipis M, Feely SME, Polke JM, Skorupinska M, Perez L, Shy RR, Laura M, Morrow JM, Moroni I, Pisciotta C, Taroni F, Vujovic D, Lloyd TE, Acsadi G, Yum SW, Lewis RA, Finkel RS, Herrmann DN, Day JW, Li J, Saporta M, Sadjadi R, Walk D, Burns J, Muntoni F, Ramchandren S, Horvath R, Johnson NE, Zuchner S, Pareyson D, Scherer SS, Rossor AM, Shy ME, Reilly MM, Inherited Neuropathies Consortium - Rare Disease Clinical Research N (2020) Natural history of Charcot-Marie-Tooth disease type 2A: a large international multicentre study. Brain : a journal of neurology 143:3589-3602.
Piscosquito G, Saveri P, Magri S, Ciano C, Di Bella D, Milani M, Taroni F, Pareyson D (2015) Mutational mechanisms in MFN2-related neuropathy: compound heterozygosity for recessive and semidominant mutations. Journal of the peripheral nervous system : JPNS 20:380-386.
Poliacikova G, Barthez M, Rival T, Aouane A, Luis NM, Richard F, Daian F, Brouilly N, Schnorrer F, Maurel-Zaffran C, Graba Y, Saurin AJ (2023) M1BP is an essential transcriptional activator of oxidative metabolism during Drosophila development. Nat Commun 14:3187.
Rival T, Macchi M, Arnaune-Pelloquin L, Poidevin M, Maillet F, Richard F, Fatmi A, Belenguer P, Royet J (2011) Inner-membrane proteins PMI/TMEM11 regulate mitochondrial morphogenesis independently of the DRP1/MFN fission/fusion pathways. EMBO reports 12:223-230.

Rocha AG, Franco A, Krezel AM, Rumsey JM, Alberti JM, Knight WC, Biris N, Zacharioudakis E, Janetka JW, Baloh RH, Kitsis RN, Mochly-Rosen D, Townsend RR, Gavathiotis E, Dorn GW, 2nd (2018) MFN2 agonists reverse mitochondrial defects in preclinical models of Charcot-Marie-Tooth disease type 2A. Science 360:336-341.

Sali A, Blundell TL (1993) Comparative protein modelling by satisfaction of spatial restraints. J Mol Biol 234:779-815.

Sandoval H, Yao CK, Chen K, Jaiswal M, Donti T, Lin YQ, Bayat V, Xiong B, Zhang K, David G, Charng WL, Yamamoto S, Duraine L, Graham BH, Bellen HJ (2014) Mitochondrial fusion but not fission regulates larval growth and synaptic development through steroid hormone production. Elife 3.

Silva Ramos E, Motori E, Bruser C, Kuhl I, Yeroslaviz A, Ruzzenente B, Kauppila JHK, Busch JD, Hultenby K, Habermann BH, Jakobs S, Larsson NG, Mourier A (2019) Mitochondrial fusion is required for regulation of mitochondrial DNA replication. PLoS genetics 15:e1008085.

Smith GA, Lin TH, Sheehan AE, Van der Goes van Naters W, Neukomm LJ, Graves HK, Bis-Brewer DM, Zuchner S, Freeman MR (2019) Glutathione S-Transferase Regulates Mitochondrial Populations in Axons through Increased Glutathione Oxidation. Neuron 103:52-65 e56.

Stavropoulos F, Sargiannidou I, Potamiti L, Kagiava A, Panayiotidis MI, Bae JH, Yeom SC, Lee JY, Kleopa KA (2021) Aberrant Mitochondrial Dynamics and Exacerbated Response to Neuroinflammation in a Novel Mouse Model of CMT2A. Int J Mol Sci 22.

Stuppia G, Rizzo F, Riboldi G, Del Bo R, Nizzardo M, Simone C, Comi GP, Bresolin N, Corti S (2015) MFN2-related neuropathies: Clinical features, molecular pathogenesis and therapeutic perspectives. Journal of the neurological sciences 356:7-18.

Tilokani L, Nagashima S, Paupe V, Prudent J (2018) Mitochondrial dynamics: overview of molecular mechanisms. Essays Biochem 62:341-360.

Tomaselli PJ, Rossor AM, Polke JM, Poh R, Blake J, Reilly MM (2016) Semi-dominant mutations in MFN2-related neuropathy and implications for genetic counselling. Journal of the peripheral nervous system : JPNS 21:52-54.

Twig G, Elorza A, Molina AJ, Mohamed H, Wikstrom JD, Walzer G, Stiles L, Haigh SE, Katz S, Las G, Alroy J, Wu M, Py BF, Yuan J, Deeney JT, Corkey BE, Shirihai OS (2008) Fission and selective fusion govern mitochondrial segregation and elimination by autophagy. The EMBO journal 27:433-446.

Verstreken P, Ly CV, Venken KJ, Koh TW, Zhou Y, Bellen HJ (2005) Synaptic mitochondria are critical for mobilization of reserve pool vesicles at Drosophila neuromuscular junctions. Neuron 47:365-378.

Wakabayashi J, Zhang Z, Wakabayashi N, Tamura Y, Fukaya M, Kensler TW, Iijima M, Sesaki H (2009) The dynamin-related GTPase Drp1 is required for embryonic and brain development in mice. The Journal of cell biology 186:805-816.

Wiederstein M, Sippl MJ (2007) ProSA-web: interactive web service for the recognition of errors in three-dimensional structures of proteins. Nucleic acids research 35:W407-410.

Yan L, Qi Y, Huang X, Yu C, Lan L, Guo X, Rao Z, Hu J, Lou Z (2018) Structural basis for GTP hydrolysis and conformational change of MFN1 in mediating membrane fusion. Nature structural & molecular biology 25:233-243.

Yun J, Puri R, Yang H, Lizzio MA, Wu C, Sheng ZH, Guo M (2014) MUL1 acts in parallel to the PINK1/parkin pathway in regulating mitofusin and compensates for loss of PINK1/parkin. Elife 3:e01958.

Ziviani E, Tao RN, Whitworth AJ (2010) Drosophila parkin requires PINK1 for mitochondrial translocation and ubiquitinates mitofusin. Proceedings of the National Academy of Sciences of the United States of America 107:5018-5023.

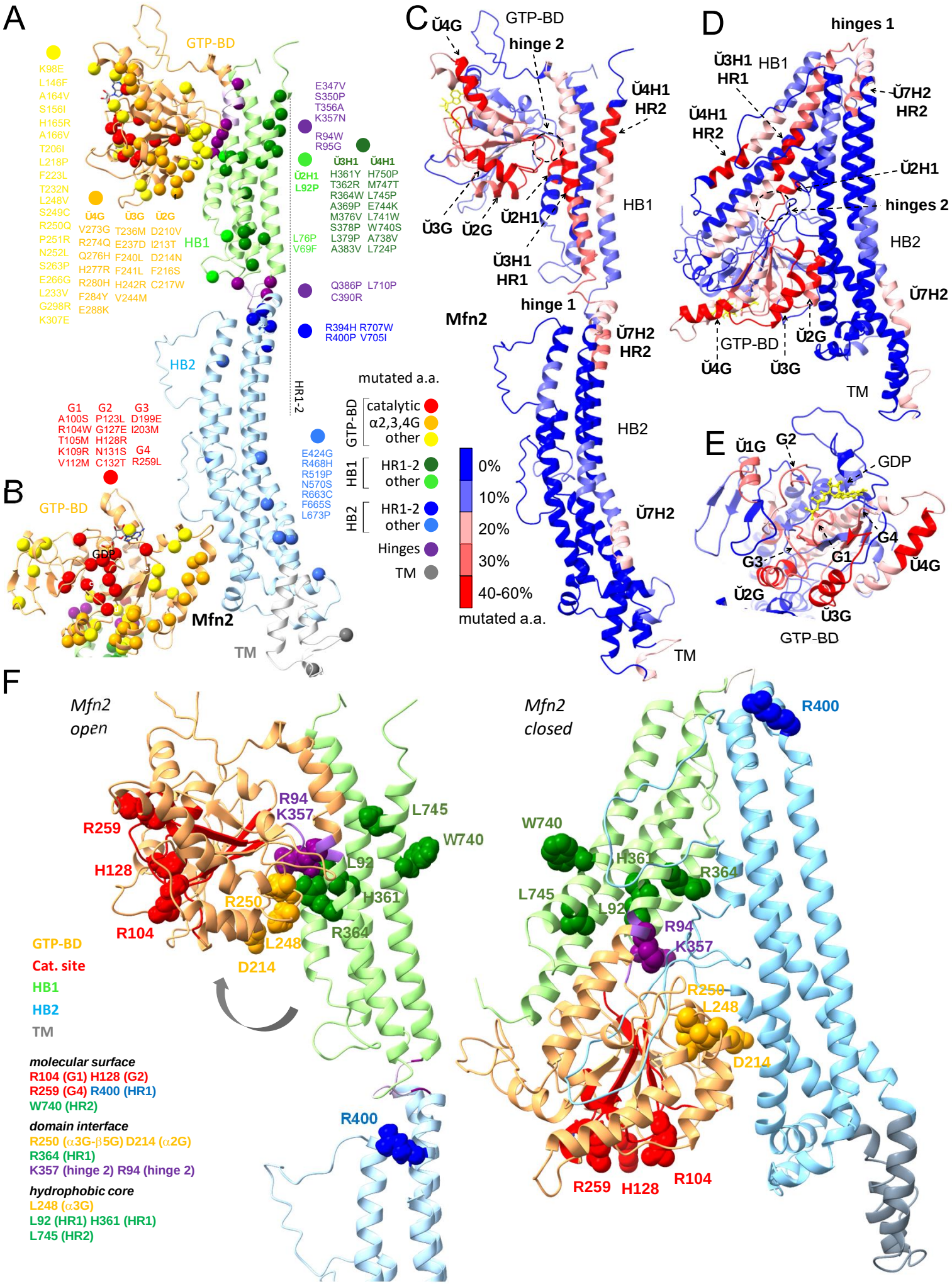

Varuk et al., Fig. 1

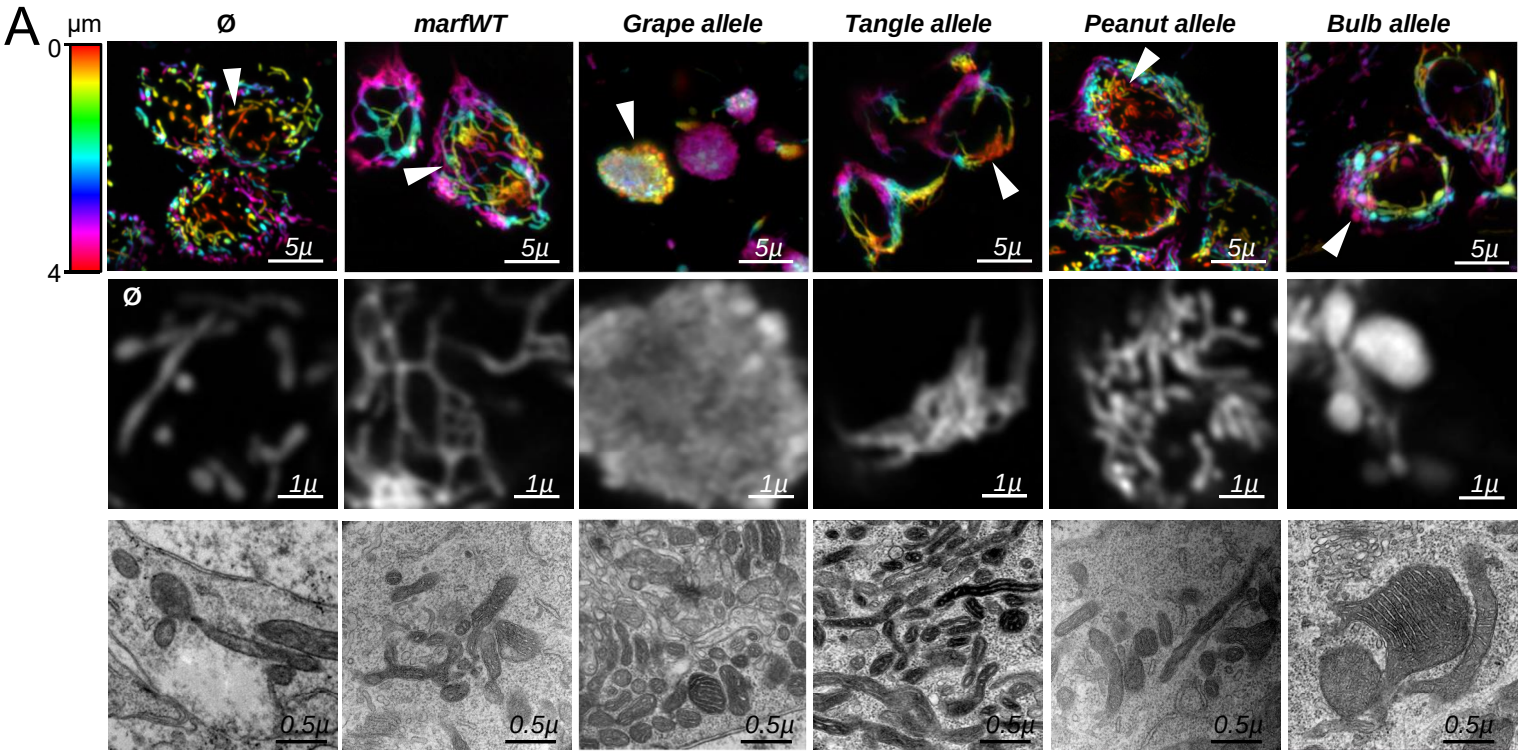

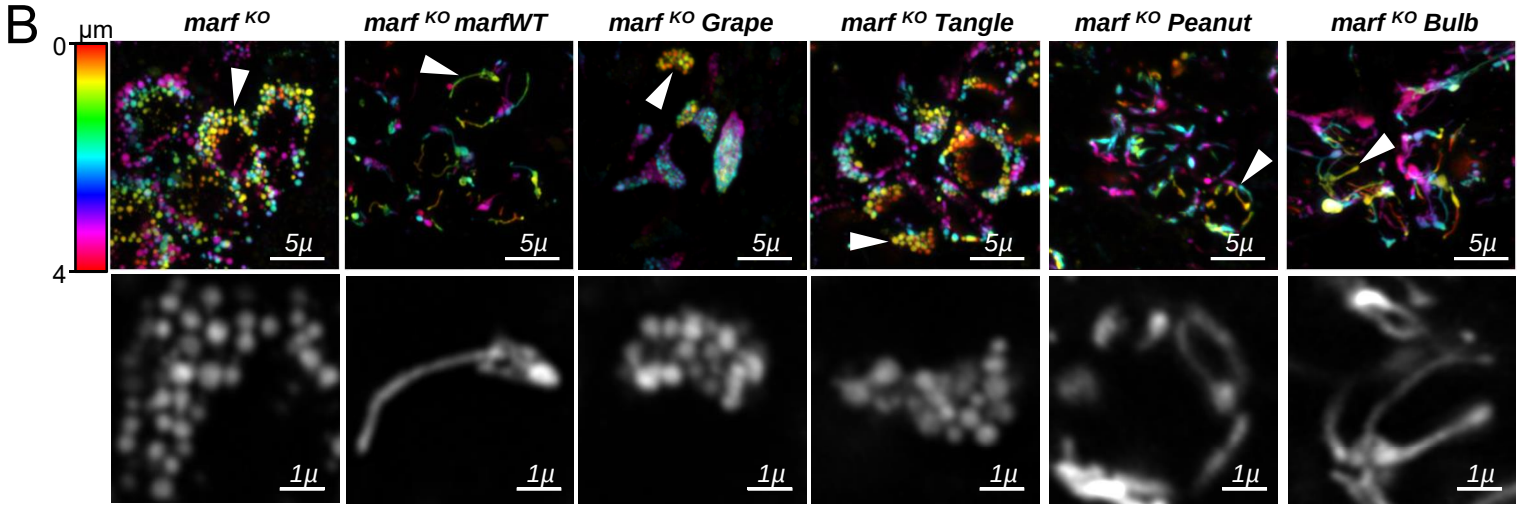

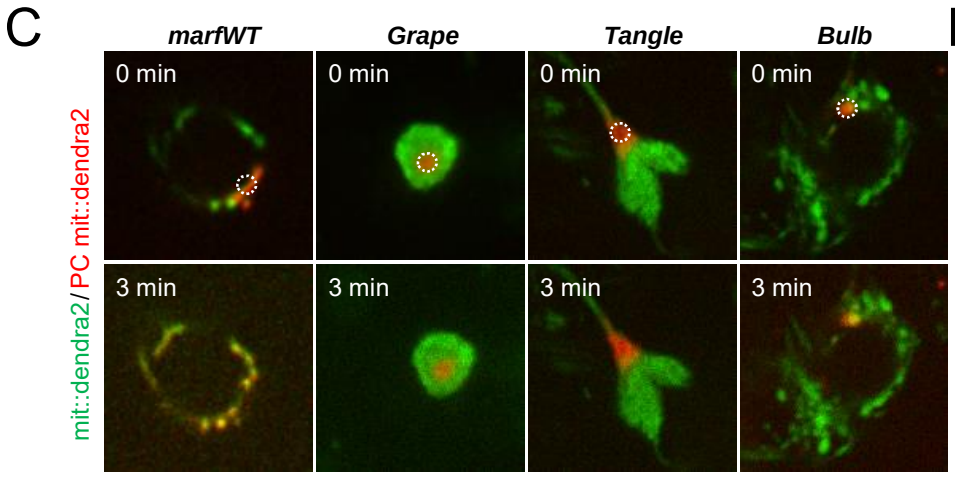

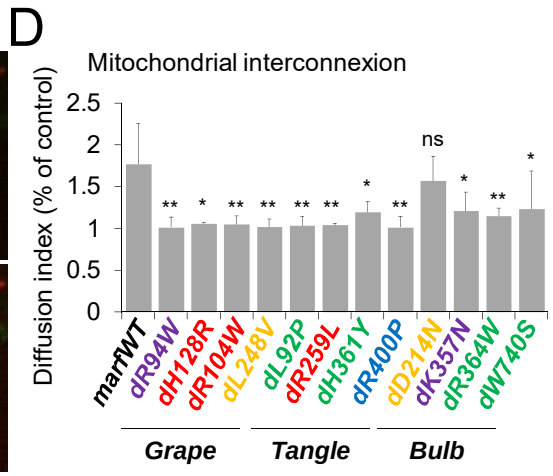

Fig. 2, Varuk *et al.*

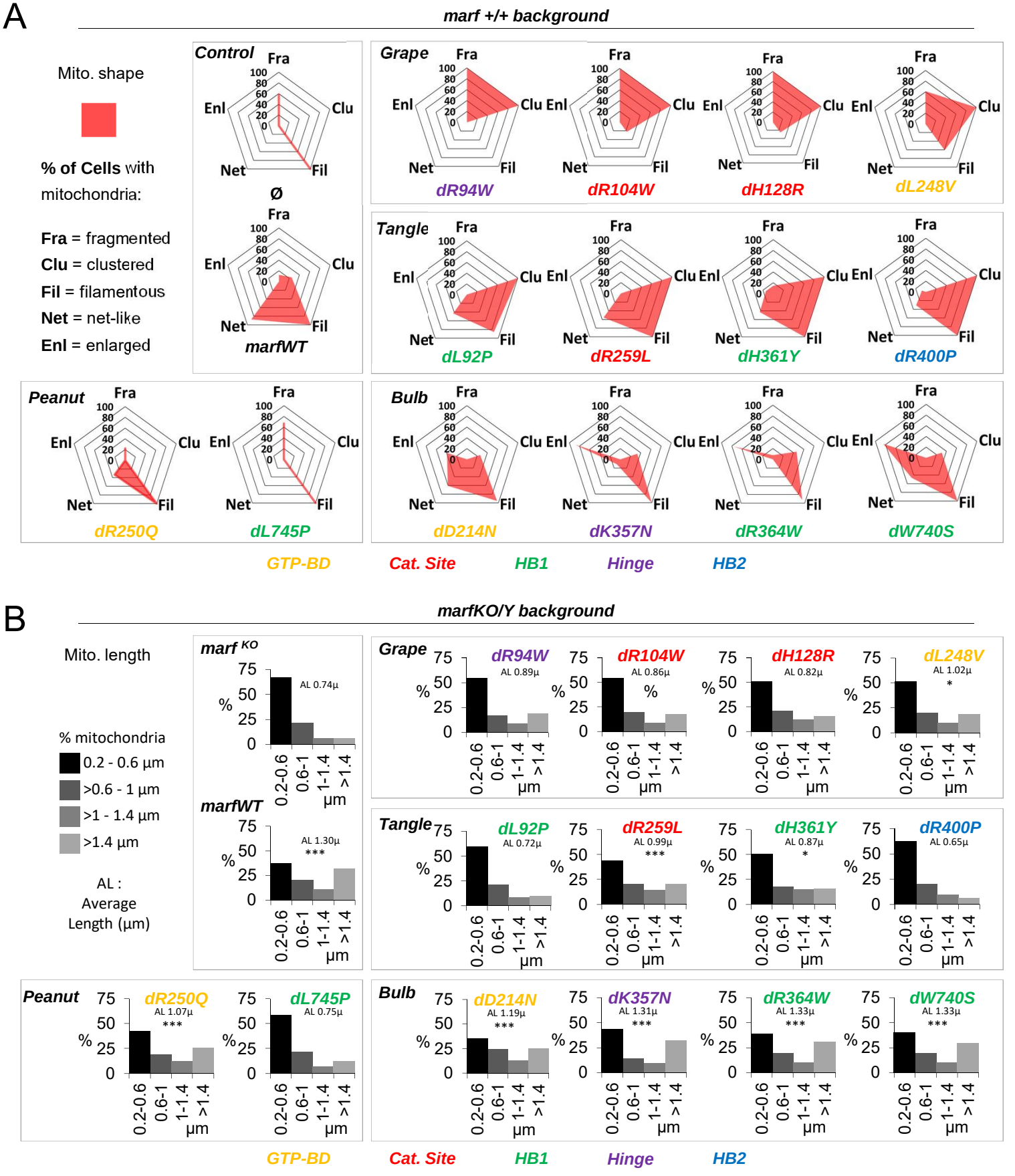

Fig. 3, Varuk *et al.*

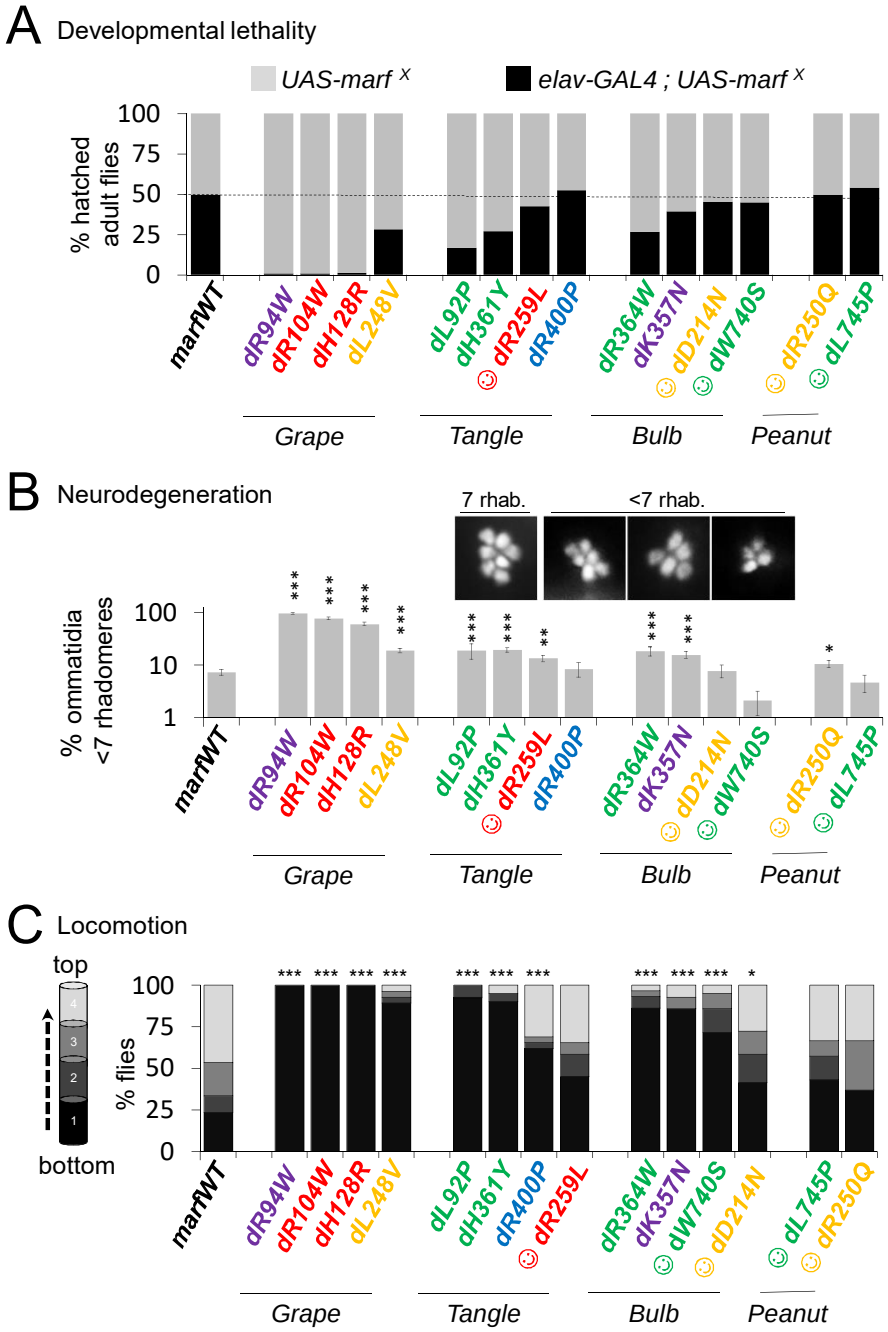

Fig. 4, Varuk *et al.*

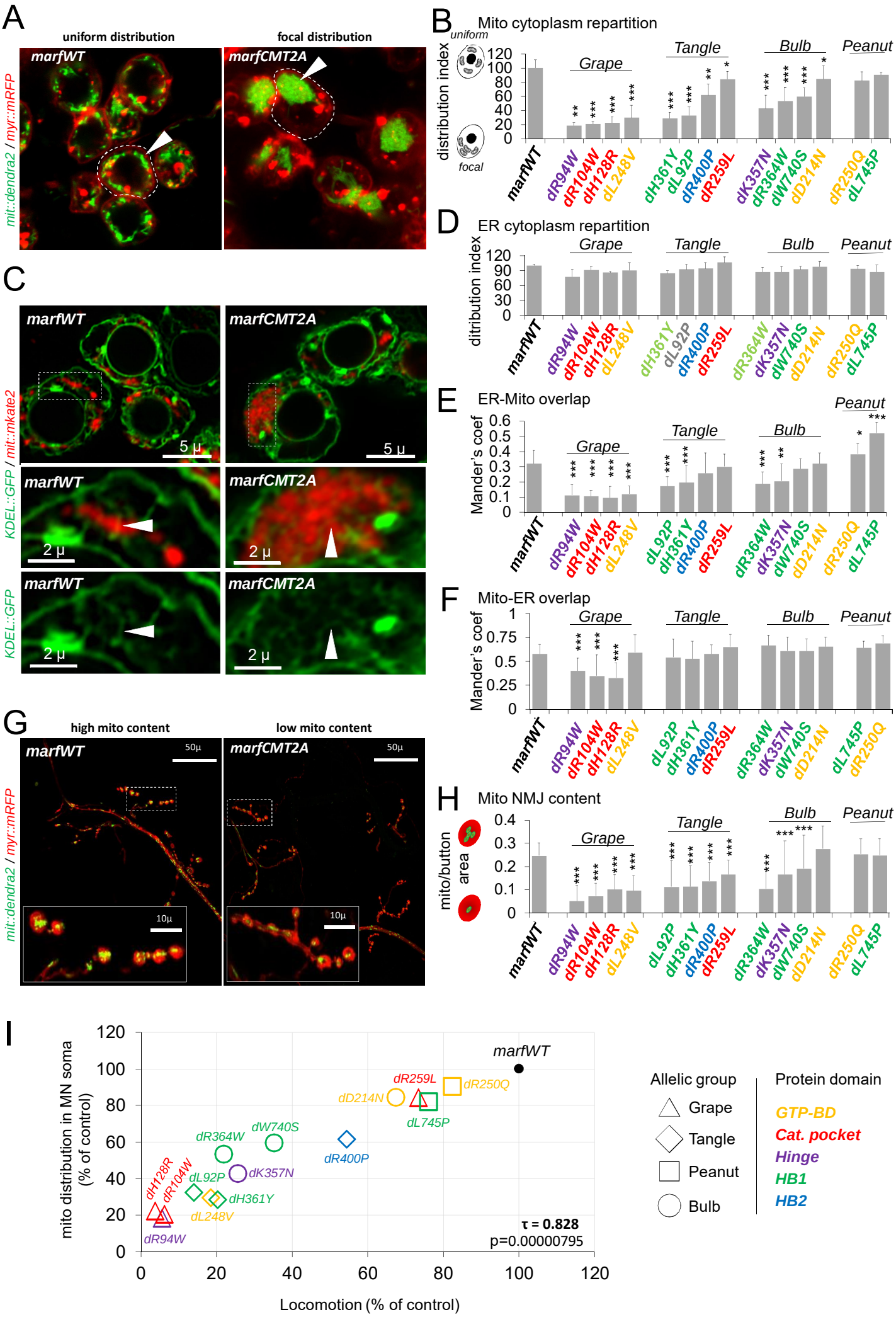

Fig. 5, Varuk *et al.*

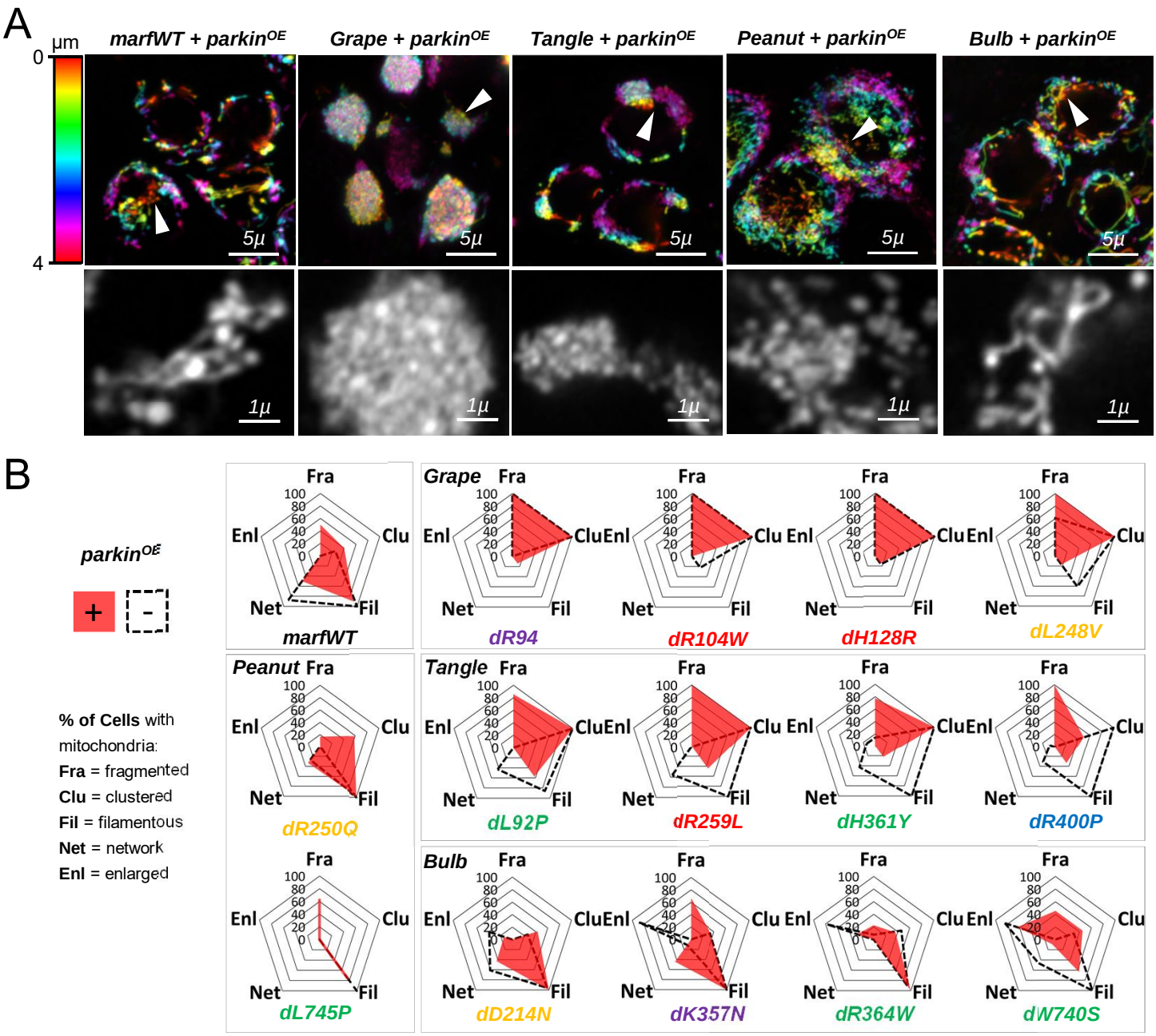

Fig. 6, Varuk *et al.*

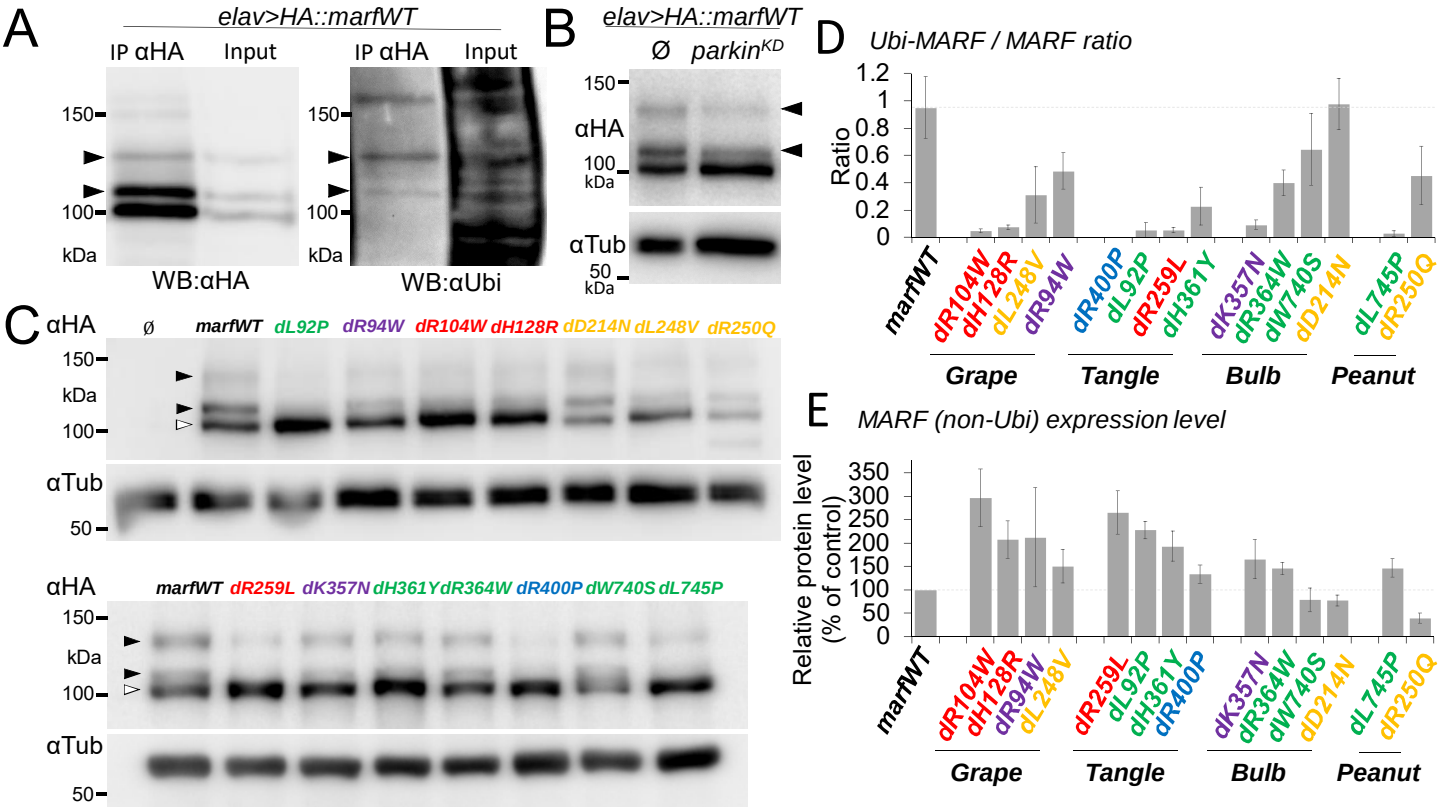

Fig. 7, Varuk *et al.*